Bioactive Materials 32 (2024) 149–163

Contents lists available at ScienceDirect

Bioactive Materials

journal homepage: www.keaipublishing.com/en/journals/bioactive-materials

Collagen fibril-like injectable hydrogels from self-assembled nanoparticles for promoting wound healing

Shanshan Li [a,1], Xiaoyun Li [a,1], Yidi Xu [b,1], Chaoran Fan [a,c], Zhong Alan Li [d], Lu Zheng [a], Bichong Luo [a], Zhi-Peng Li [b], Baofeng Lin [c], Zhen-Gang Zha [b], Huan-Tian Zhang [b,**], Xiaoying Wang [a,*]

[a] State Key Laboratory of Pulp & Paper Engineering, South China University of Technology, 381 Wushan Road, Tianhe District, Guangzhou, 510640, China
[b] Department of Bone and Joint Surgery, The First Affiliated Hospital of Jinan University, Guangzhou, 510632, China
[c] School of Chemistry and Chemical Engineering, Guangxi University, Nanning, 530004, China
[d] Department of Biomedical Engineering, The Chinese University of Hong Kong, Shatin, Hong Kong SAR, China

ARTICLE INFO

Keywords:
Injectable soft hydrogels
Collagen fibril-like structure
Self-assembled nanoparticles
Chitosan
Wound healing

ABSTRACT

Soft hydrogels are excellent candidate materials for repairing various tissue defects, yet the mechanical strength, anti-swelling properties, and biocompatibility of many soft hydrogels need to be improved. Herein, inspired by the nanostructure of collagen fibrils, we developed a strategy toward achieving a soft but tough, anti-swelling nanofibrillar hydrogel by combining the self-assembly and chemical crosslinking of nanoparticles. Specifically, the collagen fibril-like injectable hydrogel was subtly designed and fabricated by self-assembling methylacrylyl hydroxypropyl chitosan (HM) with laponite (LAP) to form nanoparticles, followed by the inter-nanoparticle bonding through photo-crosslinking. The assembly mechanism of nanoparticles was elucidated by both experimental and simulation techniques. Due to the unique structure of the crosslinked nanoparticles, the nanocomposite hydrogels exhibited low stiffness (G'< 2 kPa), high compressive strength (709 kPa), and anti-swelling (swelling ratio of 1.07 in PBS) properties. Additionally, by harnessing the photo-crosslinking ability of the nanoparticles, the nanocomposite hydrogels were processed as microgels, which can be three-dimensionally (3D) printed into complex shapes. Furthermore, we demonstrated that these nanocomposite hydrogels are highly biocompatible, biodegradability, and can effectively promote fibroblast migration and accelerate blood vessel formation during wound healing. This work presents a promising approach to develop biomimetic, nanofibrillar soft hydrogels for regenerative medicine applications.

1. Introduction

Repair and regeneration of soft tissues (e.g. skin, tendon, and muscles) remain significant clinical challenges. Soft hydrogels (<10 kPa) are a favorable material for soft tissue repair, which have been used to facilitate stem cell differentiation into target cell lineages and promote soft tissue formation [1,2]. Initially, synthetic polymer hydrogels, including polyacryl amide (PAA) [3,4], polyethylene glycol (PEG) [5], polyvinyl alcohol (PVA) [6], polydimethyl siloxane (PDMS) [7], have been adopted as the soft matrix to modulate cell behaviors. While these hydrogels have low stiffness and appropriate strength, the poor biodegradability, excessive swelling, and potential toxicity greatly restrict their clinical applications. Recently, natural polymers, like polysaccharides [8–10], peptides [11], and proteins [12–14], have been developed to fabricate soft hydrogels with higher biocompatibility. However, uncontrollable swelling and poor mechanical strength significantly limit the long-term *in vivo* applications of hydrogels, particularly in complex environments. Additionally, as implant materials, injectable hydrogels are advantageous over preformed hydrogels as they lead to better defect filling, reduced patient discomfort, and lower risk of infection [15]. To date, there has been a paucity of research into the fabrication of injectable, soft, tough, and anti-swelling natural

Peer review under responsibility of KeAi Communications Co., Ltd.
* Corresponding author.
** Corresponding author.
E-mail addresses: zhanghuantian@jnu.edu.cn (H.-T. Zhang), xyw@scut.edu.cn (X. Wang).
[1] These authors contributed equally to this work.

https://doi.org/10.1016/j.bioactmat.2023.09.012
Received 9 May 2023; Received in revised form 24 August 2023; Accepted 18 September 2023

polymer hydrogels.

The extracellular matrix (ECM) of most soft tissues is mainly composed of a network of sturdy and water-insoluble fibrillar proteins, such as collagen, and thus has low swelling and high mechanical strength [16]. This is due to the major role played by the collagen fibrils in collagen, which are assembled from collagen molecules [17,18]. Their hydrophobic groups could reduce the ability of the obtained fibrillar network to bind to water. Moreover, owing to their hierarchical filamentous structure with transverse striations, improved energy dissipation could be realized by utilizing internal collagen molecules through helical deformation and relative slip [17]. Inspired by these, some biomimetic nanofibrillar hydrogels have been reported, which were generally formed by hierarchical assembly of molecular or nano-colloidal building blocks into fibrils followed by crosslinking [19–22]. They have tunable stiffness, good mechanical properties, and fibrillar structure, but most of them do not display multiple energy dissipation mechanisms and lack injectability due to uncontrolled self-assembly and crosslinking. In addition, only a limited number of studies examined the swelling properties.

Hydroxypropyl chitosan (HCS), an important chitosan derivative with good water solubility, amphiphilicity, biocompatibility and biodegradability, is often used in pharmaceuticals, skin repair, and tissue engineering [23,24]. HCS can form aggregates in aqueous solution by self-assembly, due to its hydrophobic interaction (acetyl group and glycosides) and intermolecular hydrogen bonding [23,25]. Its amino can be used to introduce vinyl groups to obtain injectable photo-crosslinking hydrogels with spatiotemporal controllability. Hence, HCS could be a promising candidate for forming injectable nanofibrillar hydrogels by chemical crosslinking between aggregates, which, however, has been rarely reported. Laponite (LAP), a 2D nanosized silicate disc, exhibits permanent negative charge on the surface and positive charge on the rim, which readily binds electrostatically to positively charged chitosan [26,27]. Therefore, we hypothesize that the introduction of LAP can enhance the cohesion of HCS aggregates, offering the possibility of developing injectable, soft, tough, and swell-resistant hydrogels.

Herein, by emulating the nanostructure and amphiphilicity of collagen fibres, we proposed a combined self-assembly and chemical cross-linking strategy for the preparation of injectable, biocompatible, soft (G'< 2 kPa), compression-resistant (compressive strength of 709 kPa), and anti-swelling (swelling ratio of 1.07 in PBS) hydrogels from natural polymers. The self-assembled nanoparticles were formed by the interaction of methylacrylyl HCS (HM) with LAP, which then bonded with each other by photo-crosslinking to form a collagen fibril-like nanostructured hydrogel (Scheme 1). In addition, we explored the effects of processing factors such as methylacrylyl group (MA) substitution degrees of HM and the amount of LAP added to the hydrogels' physical properties and drug release performance. Furthermore, we examined the biocompatibility of the hydrogels and the printability of their reprocessed microgels. Finally, the effects of HM/LAP (HML) hydrogels on skin regeneration were evaluated both *in vitro* and *in vivo*, which revealed their great potential in soft-tissue engineering applications. This work provides a promising strategy for the development of biomimetic nanofibrillar hydrogels and soft hydrogels for long-term biomedical applications such as wound dressing.

2. Materials and methods

2.1. Materials

HCS (MW ~100 kDa) was purchased from Shanghai Shifeng Biological Technology Co., Ltd. Laponite XLG (LAP) was purchased from BYK Additives & Instruments, Germany. Methacrylic anhydride, Irgacure 2959, phosphate buffer solution (PBS), and pyrene were obtained from Macklin Biotechnology Co., Ltd, China. Bovine serum albumin (BSA, 68 kDa) was obtained from BioFroxx, Germany. BCA Protein Assay Kit was purchased from Beijing Solarbio Science & Technology Co. Ltd, China. Deionized water (DI water) from a Milli-Q water system was used in all experiments.

2.2. Synthesis and characterization of HM

HM was synthesized according to the previous report of methacrylated gelatin with appropriate modification [28]. 5 g of HCS was added to 200 mL of PBS (pH = 7.4) kept stirring to the homogeneous solution,

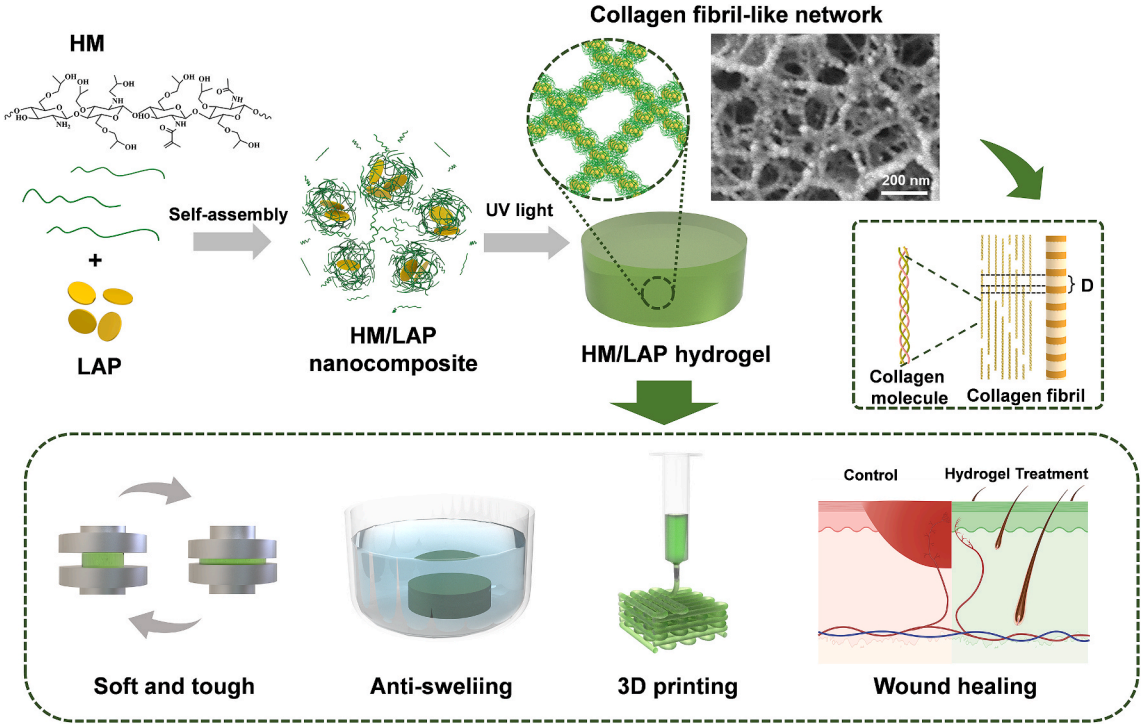

Scheme 1. Schematic illustration of the preparation and properties of collagen fibril-like HML nanocomposite hydrogels in tissue engineering.

and heated up to 50 °C. Then, methacrylic anhydride was slowly (0.5 mL/min) added to the above solution and kept stirring at 50 °C for 4 h. The mixture was then cooled to room temperature and dialyzed against PBS using 10,000 MWCO membrane to remove unreacted methacrylic anhydride at 45 °C for 5 d. After dialysis in DI water for 1 d, the HM solution was freeze-dried. 0.375 mL, 0.75 mL, 1.5 mL, and 3.0 mL of methacrylic anhydride were used to fabricate HM with different degrees of substitution of methylacrylyl group (DS_{MA}) and marked as HM_1, HM_2, HM_3, and HM_4, respectively.

The HM structure was determined using FT-IR spectroscopy (TENSOR27, Bruker) and ^{1}H-NMR spectrometry (Bruker Avance III HD, 600 MHz, D_2O).

The DS_{MA} of HM was measured by the ninhydrin method [29]. For ninhydrin measurement, 10 mg of HM was dissolved in 0.5 mL of acetic acid/sodium acetate buffer (4 M, pH 5.5), and then mixed with 0.5 mL ninhydrin reagent. After reacting at 100 °C for 20 min, the mixture was cool down and the absorbance at 570 nm was measured. To generate a standard curve, unmodified HCS was serially diluted in acetic acid/-sodium acetate buffer from 0 to 10 mg/mL in increments of 1 mg/mL in triplicate.

2.3. Preparation of HML nanocomposite hydrogel

Various amounts of LAP (2, 5, 7.5, 10, and 20 mg/mL) dispersion were prepared in 0.5% Irgacure 2959 solution. 40 mg of HM was added to 1 mL of LAP dispersion and stirred until completely dissolved to acquire the HML nanocomposite. The HML nanocomposite was labeled as HM_tL_x, where t and x are the serial number of HM with different DS_{MA} and concentrations of LAP dispersion (2, 5, 7.5, 10, and 20 mg/mL), respectively. The nanocomposite was then defoamed by centrifugation and irradiated by UV light (365 nm, 10 mW cm^{-2}) for 2 min to form the HML nanocomposite hydrogel (HM_tL_x hydrogel).

2.4. Characterization of HML nanocomposite hydrogel

The UV–vis transmittance spectra of the nanocomposite were obtained by UV-1800 spectrophotometer (Shimadzu, Japan). X-ray photoelectron spectroscopy (XPS) measurements were taken by Thermo Scientific NEXSA spectrometer using Al Kα radiation (hυ = 1486.6 eV). The morphology of the nanocomposite was observed by scanning electron microscope (SEM, Merlin, Zeiss, Germany). Further, cryo-SEM (JSM-7900F, JEOL, Japan) was used to investigate the ultrastructure of the hydrogels.

The hydrodynamic diameters and zeta potentials of nanocomposites with different compositions were characterized by Nanoparticles Analyzer (HORIBA SZ-100Z, Japan). Due to the low transmittance of the original nanocomposite, the Analyzer cannot detect it. There is another way to evaluate the nanocomposites: 4 mg of HM was added to 1 mL of LAP dispersion (0.2, 0.5, 1.0, 2.0 mg/mL) and stirred until completely dissolved, which can indirectly reflect the formation of HML nanocomposite. Considering the critical micelle concentration (CMC) of HM_2, 5 mg/mL was used as the tested concentration of HM_2 in hydrodynamic diameters measurement.

2.5. Molecular dynamic simulations

Molecular models were built using Materials Studio 2017, with a 100-unit structure of HM molecule, and a layer sepiolite supercell (u = 12, v = 4). The sepiolite and HM molecular models were geometrically optimized using the Geometry Optimization method in the Forcite module (COMPASS II force, Ultra-fine). The optimized HM was added to the sepiolite surface using the layering tool (vacuum layer set to 100) and the kinetic calculations were run. Then the Dynamics option in the Forcite module (Ultra-fine accuracy), and NVT (canonical ensemble) were selected, and the total simulation time was 200 ps. The thermostat selected Andersen for dynamic simulation at 298 K. The interaction energy of HM with the sepiolite surface was calculated by Equation (1):

$$E_{Interaction} = E_{total} - \left(E_{Sepiolite} + E_{HM}\right) \quad (1)$$

E_{total} is the energy of sepiolite and HM, $E_{Sepiolite}$ is the energy of sepiolite without HM, and E_{HM} is the energy of HM without sepiolite. These calculations were single-point energies and were performed with the removal of constraints.

2.6. Physical properties

To measure the swelling properties of nanocomposite hydrogels in different environments, all hydrogels (W_d) were soaked in H_2O/PBS/DMEM at 37 °C, respectively. At a designed time (t = 0, 2, 4, 6, 10, 24, 36, 48 h), the wet weight (W_t) of the hydrogels was measured after removing solvent on the surface by wiping gently using a filter paper. The weight swelling ratio of hydrogels was calculated by Equation (2):

$$\text{Swelling ratio} = \frac{W_t}{W_0} \quad (2)$$

Mechanical properties were detected by a Universal Testing Machine (INSTRON VS81452323RE). The compressive strength was measured on samples with a diameter = 10 mm and a thickness = 3.0 mm at a speed of 1 mm min^{-1}. Additionally, the 3D printed hydrogel (diameter = 10 mm, thickness = 3.0 mm, line distance = 0.8 mm, layer height = 0.3 mm) used for mechanical measurement was printed by a 21 G needle. The compressive modulus was calculated using the slope of the stress-strain curve with a strain of 0.05–0.15 mm/mm. The cycle compression data was taken for HM_2L_5 gel in three strain ranges (0–60%, 0–65%, and 0–70%) for 5 cycles, which was processed to monitor energy dissipated. Five replicates were used for each hydrogel composition.

Rheological measurements were conducted on a TA Instruments ARES-G2 Rheometer equipped with a 25 mm/8 mm parallel plate geometry at 25 °C in a humid atmosphere with a gap distance of 1 mm. Rheological properties of hydrogels were examined by amplitude sweep (0.1–1000% strain, 1 Hz) and frequency sweeps oscillatory shear (0.1–100 rad s^{-1}, 1% strain) to evaluate storage and loss modulus, yield point.

To determine the degradation characteristics of the hydrogels, the indicated samples were incubated in lysozyme solution (1.0 mg/mL, dissolved in PBS) for 7, 14, 21, and 28 d. The weight (W_t) of the hydrogels was measured after multiple rinsing in DI water, followed by freeze-drying. The degradation ratio of hydrogels was calculated by Equation (3):

$$\text{Degradation ratio} = \frac{W_t}{W_0} \quad (3)$$

2.7. In vitro drug release performance

For fabricating BSA-loaded HML nanocomposite hydrogels, BSA was dissolved in each HML nanocomposite at a concentration of 1 mg/mL and stirred for 12 h, followed by UV irradiation. 0.3 g of BSA-loaded hydrogels was immersed with 1.2 mL PBS and placed in a 37 °C shaker. 100 μL of the liquid was aspirated at a designed time point for sampling, and 100 μL of fresh PBS was replaced. The collected sample liquid was stored frozen at −20 °C. After day 7, the BSA concentrations in the release media were determined using the BCA assay kit by the Microplate Reader (Thermo, Multiskan, USA).

2.8. Preparation and characterization of HML nanocomposite microgels

To create printable microgels, bulk nanocomposite hydrogels were made inside a 5 mL syringe and manually pressed through a 400-mesh nylon sieve and repeated one more time. HM_2L_5 gel was selected as the experimental object. The rheological behaviors of microgels were also investigated in shear rate sweeps (0.1–500 s^{-1}), besides amplitude

sweep and frequency sweeps. For shear recovery properties, samples were exposed to repeating cycles of alternating phases of strain (1 Hz, 1%, and 500% strain, 300 s).

The 3D printing process was performed in a desktop bioprinter (BioMaker, Sunp Biotech, Beijing, China). Briefly, microgels were defoamed by centrifugation and then loaded into a print syringe equipped with a 22 G needle. The extrusion speed and moving speed were coordinated to deliver continuous filaments. After printing, the printed constructs were treated with UV light (365 nm, 10 mW cm^{-2}) for 2 min in an N_2 atmosphere to avoid oxygen inhibition. To explore the shape fidelity of different microgels, a hollow cylinder (height = 10 mm, diameter = 10 mm, layer height = 200 μm) was set and printed from the microgels. The actual height of the cylinder was measured, and each microgel was tested at least three times.

2.9. In vitro biocompatibility

Human bone marrow mesenchymal stem cells (hMSCs) were used to evaluate the cytotoxicity of the nanocomposites and hydrogels. Pre-seeded hMSCs were treated with different concentrations of HM_2 solution (0.1–10 mg/mL), LAP solution (0.001–5 mg/mL), and HM_2L_5 solution (0.1125–11.25 mg/mL) for 1 d and 3 d. Then the cell viability was analyzed by the CCK-8 kit assay. Additionally, hMSCs were co-incubated with the hydrogels of 50 mg/mL for 1, 3, and 5 d, respectively, and were tested by lived/dead staining and CCK-8 kit assay.

HUVECs and L929 cells were also used to detect the cell viability of the hydrogels through the CCK-8 kit assay. HUVECs and L929 cells were cultured in Endothelial Cell Medium (ECM) and DMEM, respectively. Briefly, 3×10^3 cells/well of HUVECs and L929 cells were seeded onto 96-well plates and then treated with different hydrogel extracts (50 mg hydrogel in 1 mL medium). After incubation for 1, 3, and 5 d, CCK-8 solution was added and incubated for 2 h, and the cell absorbance was detected at 450 nm by a microplate reader. Cell viability was calculated according to Equation (4):

$$\text{Cell viability } (\%) = \frac{\text{Absorbance}_{Sample}}{\text{Absorbance}_{Control}} \times 100\% \quad (4)$$

The *in vitro* hemolysis ratio of nanocomposite was measured. HM_2 solution (10 mg/mL), LAP suspension (1.25 mg/mL), and HM_2L_5 nanocomposite (11.25 mg/mL) were diluted to corresponding concentrations by PBS. Then, 200 μL of erythrocyte diluent was mixed with 800 μL of the sample suspension and then incubated at 37 °C for 1 h. After centrifuging at 3000 rpm for 5 min, the absorbance of the supernatant (A_S) was read at 405 nm in a microplate reader. DI water and PBS were used as the positive (A_P) and negative control (A_N), respectively. The hemolysis ratio (%) was calculated according to Equation (5):

$$\text{Hemolysis ratio } (\%) = \frac{A_S - A_N}{A_P - A_N} \times 100\% \quad (5)$$

Tube formation assay was used to measure the capillary tube formation of hydrogel. Matrigel and FBS-free DMEM were mixed 1:1. Approximately 50 μL of Matrigel (BD Biocoat) was covered in the wells in 96-well plates and incubated for 40 min. Then, 3×10^3 HUVECs were seeded into Matrigel-covered plates and treated with different hydrogel extracts. After 4 h, capillary-like structures were captured under a light microscope (Leica, Germany).

Scratch assay was used to evaluate the cell migration effects of the different hydrogels on L929 dermal fibroblasts. L929 cells were seeded on the 6-well plates at a density of 5×10^5 cells/well. After the cell achieved confluence, a scratch was made using a pipette tip of 200 μL. Different low-FBS hydrogel extracts were placed in the wells and allowed to incubate for another 24 h. Photographs were obtained using a light microscope (Leica, Germany) and analyzed by Image-J. A_0 is the area of the initial scratch, and A_{24} is the area after sample treatment for 24 h. The migration ability was quantified from the images by Equation (6):

$$\text{Migration area rate } (\%) = \frac{A_0 - A_{24}}{A_0} \times 100\% \quad (6)$$

2.10. In vivo wound healing

All animal studies were approved by the Jinan University Animal Care and Use Committee (permit No. 20211216-15). A full-thickness wound model was established to assess the effect of HM_2 hydrogel, HM_2L_5 hydrogel, and HM_2L_5 microgels on wound healing. Briefly, a round full-thickness cutaneous wound (diameter = 6 mm) was created on the back of the mice. Then, the mice were randomly divided into three groups (n = 10), which were then treated with control, HM_2 hydrogel, HM_2L_5 hydrogel, and HM_2L_5 microgels, respectively. To observe the wound healing process, the wound photographs were captured with a digital camera on days 0, 3, 7, and 11 d. The wound area on day 0 is marked as A_0, and the wound area after hydrogel treatment on day t is marked as A_t. The wound healing rate (%) was calculated by Equation (7), as previously described [30].

$$\text{Wound healing rate } (\%) = \frac{A_0 - A_t}{A_0} \times 100\% \quad (7)$$

2.11. Histological analysis and immunofluorescence staining

On day 7 and day 11, the wound tissues with the surrounding tissues of the mice were dissected after euthanasia. The samples were fixed in 10% buffered formalin (Servicebio, China), then were embedded in paraffin blocks, and sectioned into sequential 6 μm-thick sections. The sections were stained with hematoxylin-eosin (H&E) and Masson's trichrome for histological analyses. Additionally, the toxicological effects of HM_2L_5 nanocomposites on major organs (heart, liver, spleen, lung, and kidney) were also evaluated by the H&E staining.

For immunofluorescence staining, the tissue sections were processed by deparaffinization, antigen-retrieval (citrated buffer, heat-induced), permeabilization (0.3% Triton PBST), and antigen blocking (goat serum, Solarbio, China). Moreover, sections were first incubated with primary antibodies against α-SMA (1:1000, Servicebio, China, GB13044) and CD31 (1:1000, R&D, USA, AF3628), followed by the incubation with secondary antibodies (IF488-Tyramide, G1226-1, IF555-Tyramide, G1226-2, Servicebio, China), respectively. DAPI was employed to visualize nuclei. Finally, photographs were captured via Zeiss LSM 880 and analyzed by Image-J software. The vascular maturation index was assessed by calculating the total number of CD31+α-SMA + areas and areas positive for CD31 alone in double-stained (CD31/α-SMA).

2.12. In vivo degradation evaluation

First, a 2.5 cm incision was made on the back of each 8-week-old male mouse (n = 3), immediately followed by the subcutaneous implantation with HM_2 hydrogel, HM_2L_5 hydrogel and HM_2L_5 microgels (40 mg), respectively. Then, the mices were sacrificed 1 and 2 weeks post-surgery and implants and surrounding tissues were collected for histological evaluation.

2.13. Statistical analysis

Three independent experiments were carried out for each analysis unless stated otherwise. Data are presented as the means ± standard deviations (SD). All results were analyzed for statistical significance using GraphPad Prism 8 software. When the confidence interval was less than 5% ($p < 0.05$), the differences between means were considered significant.

3. Results and discussion

3.1. Preparation and characterization of HML nanocomposites

HM was synthesized by the direct reaction of HCS with MA in PBS (pH = 7.4) at 50 °C, as shown in Fig. S1a. This reaction introduced methacrylate substitution groups on the reactive amine of HCS to endow HCS with UV crosslinking ability. The chemical structures of HCS were confirmed by ^{1}H NMR spectra and FT-IR spectra (Figs. S1b–c). HCS had a high degree of substitution (DS) of hydroxypropyl, which was up to 2.27 calculated by the integral area ratio. As previously reported, HCS with high DS of hydroxypropyl could reduce the surface tension, indirectly demonstrating its amphiphilic nature and self-assembly ability [31,32]. Moreover, both ^{1}H NMR spectra and FT-IR spectra of HM (HM_1, HM_2, HM_3, HM_4) indicated that HM with different DS_{MA} was successfully synthesized, while the signals of MA groups appeared and increased with the addition of methacrylic anhydride. Calculated with ninhydrin method, the DS_{MA} of HM_1, HM_2, HM_3, and HM_4 to amino was 53%, 67%, 75% and 82%, respectively.

The HML nanocomposites, prepared by a simple mix of the aqueous LAP solution with different amounts of HM, were defined as HM_tL_x, with t indicating different DS_{MA} of HM (1, 2, 3, and 4), and x denoting different concentrations of LAP dispersion (2, 5, 7.5, 10, and 20 mg/mL). Herein, HM_2 was chosen as a representative to assess the influence of different LAP concentrations on the properties of nanocomposites and hydrogels. Of significance, the appearance of nanocomposites changed from transparent to translucent and then to opaque upon the addition of an increasing amount of LAP (Fig. 1a(i)). This appearance was further confirmed by the UV–vis absorption spectra (Fig. 1b). In addition, the HM_2 solution showed the Tyndall effect due to its superior colloidal stability, while the intensity of scattered light changed with increasing LAP concentration in the mixtures (Fig. 1a(ii)). Consistent with this, HM_2L_5, $HM_2L_{7.5}$, HM_2L_{10}, and HM_2L_{20} exhibited different degrees of phase separation after centrifugation, but HM_2L_2 did not (Fig. 1a(iii)).

To demonstrate the formation of nanoparticles in the nanocomposite, a Nanoparticles Analyzer was utilized. As shown in Fig. 1c, the average hydrodynamic sizes of the dilute HML nanocomposites gradually decreased with an increase in LAP content. Additionally, XPS spectra confirmed the presence of LAP in the nanocomposites (Fig. 1d). The dilute HM_2 solution exhibited three particle size peaks (Figs. S2a–b), presumably referring to free HM molecular chains (Peak 1, 3.52 ± 0.88 nm), HM nanoparticles (Peak 2, 28.49 ± 3.98 nm), and aggregates formed by the nanoparticles (Peak 3, >1000 nm), respectively. Harnessing the spin-coating method, we prepared HM_2 and HML nano-films on the silicon slice, as visualized by the scanning electron microscopy (SEM) in Fig. 1e and Fig. S3. HM_2 alone exhibited uniform spherical nanoparticles (size around 20 nm) as a result of its hydrophobic effect from acetyl and glycosidic rings, as well as the hydrogen bonding from hydroxypropyl, amino, and hydroxyl [23], which is consistent with Fig. S2. After adding 2 mg/mL LAP, the size of nanoparticles increased to over 100 nm. With the content of LAP increased, more composite material remained on the silicon slice, along with wrinkles caused by drying, but fine particles can still be seen attached to the surface. As expected, the diameter of the nanoparticles decreased, which is consistent with the above results. The nanoparticles displayed a smaller diameter in the SEM images than the hydrodynamic diameters revealed by the Nanoparticle Analyzer, possibly due to the dilution of the reactant concentrations, which inhibited the formation of stable physical entanglement by free HM chains, as well as the agglomeration of nanocomposites in the latter. In parallel, the structure of HM_2, LAP, and HM_2L_5 after freeze-drying was characterized by SEM and was shown in Fig. S3. As expected, the addition of LAP facilitated the formation of micropores on the nanocomposite, which is indicative of a more compact network with a higher degree of physical cross-linking. In addition, accumulated pellets were found in the cross-section of the nanocomposite, which confirmed the formation of nanoparticles.

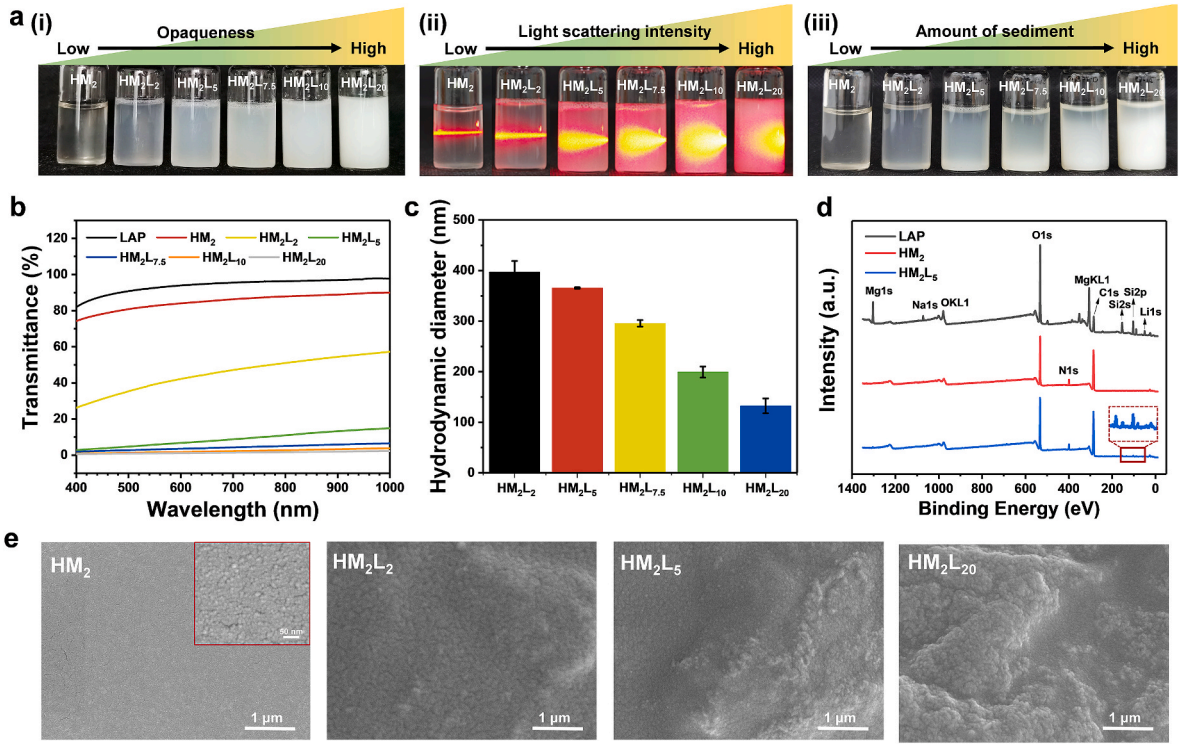

Fig. 1. Characterization of HML-based nanocomposites. a) Representative images of a series of HML nanocomposites containing different concentrations of LAP (left to right: 0, 2, 5, 7.5, 10, and 20 mg/mL), showing (i) as-synthesized samples, (ii) Tyndall effect, and (iii) samples after centrifugation at 4000 rad/min for 20 min. b) UV–vis absorption spectra and c) hydrodynamic diameters of the dilute HML nanocomposites. d) XPS spectra of representative HML nanocomposites. e) SEM images of HML nanocomposites after spin-coating.

Overall, we have successfully established HML nanocomposites.

Next, we sought to investigate the formation mechanism of the aforementioned HML nanocomposites. As shown in Fig. 2a, the HM_2 solution harbored positive zeta potential values (+26.2 mV), while LAP itself exhibited negative zeta potential values (– 35.8 mV). The addition of LAP reduced the zeta potential value of the indicated nanocomposites in a dose-dependent manner, from +26.2 mV for HM_2 to +17.4 mV, +14.7 mV, +8.4 mV, +6.4 mV, and +2.6 mV for HM_2L_2, HM_2L_5, $HM_2L_{7.5}$, HM_2L_{10} and HM_2L_{20}, respectively, indicative of the formation of nanoparticles through electrostatic self-assembly of negative LAP wrapped by positively charged HM. In addition, the aggregation behavior of HM in an aqueous medium was determined using pyrene as a fluorescence probe. The critical micelle concentration (CMC) of HM_2 was 4.31 mg/mL (Fig. 2b), suggesting that HM had amphiphilicity and

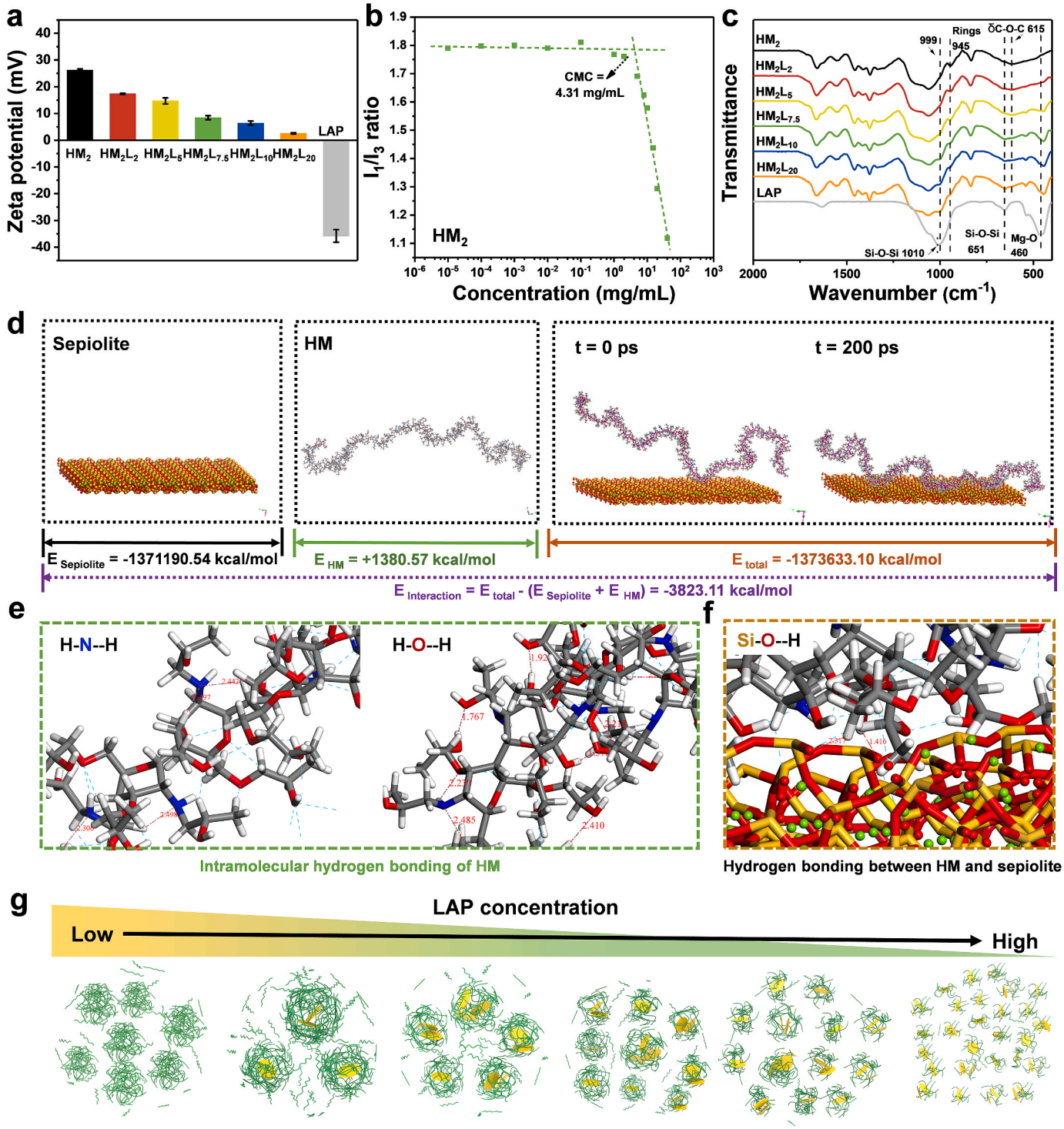

Fig. 2. Interactions between HM and LAP. a) Zeta potential of a series of HML nanocomposites containing different concentrations of LAP. b) Variation of pyrene polarity parameter I_1/I_3 with HM_2 polymer concentration. c) FT-IR spectra of HML nanocomposites and their constituents. d) Atomistic molecular dynamics simulations of sepiolite and HM_2 assembly. e) Simulation of hydrogen bonding interactions within HM and between HM and sepiolite. g) Schematic illustration of nanoparticle size evolution with increasing concentrations of LAP.

could self-assemble at a concentration of 40 mg/mL. In the FT-IR spectra (Fig. 2c), all nanocomposites displayed bands corresponding to Si–O stretching, Si–O–Si stretching, and Si–O bending at 999 cm^{-1}, 657 cm^{-1}, and 443 cm^{-1}, respectively, which had an obvious shift compared with bare LAP (1010 cm^{-1}, 651 cm^{-1}, and 460 cm^{-1}). Further, the C–O stretching bands at 1373 cm^{-1}, C–H bending band at 831 cm^{-1}, and C–N stretching bands at 1409 cm^{-1} in the nanocomposite all exhibited blue shift compared with those of HM_2 (1379 cm^{-1}, 837 cm^{-1}, and 1415 cm^{-1}). These results suggest that LAP was introduced into the HM and the hydrogen bonds were formed between HM chains and LAP [33]. Moreover, the intensities of the rings' stretching band at 945 $cm^{-1}$and C–O–C bending band at 615 cm^{-1} in the nanocomposites were weakened with increasing LAP concentration, possibly due to more absorption of HM_2 backbones on the LAP surface. Collectively, these results suggest that the nanoparticles were formed by electrostatic interaction and hydrogen bonding between LAP and HM and confirmed the self-assembly ability of HM.

Further, molecular dynamics (MD) simulations were conducted to investigate the underlying mechanism of HML nanoparticle formation. Since the structure of LAP is not available in the database, sepiolite ($Mg_4Si_6O_{15}(OH)_2$–$6H_2O$), which has a similar structure to LAP, was chosen for the simulations and used to calculate the interactions between clay and HM. Although slight structural differences exist between sepiolite and LAP, using the sepiolite structure for LAP in MD simulation was acceptable in related studies [34]. All MD simulations were performed using Forcite code and COMPASS II force field, and the kinetics-related parameters were calculated according to previous studies [34]. As shown in Fig. 2d and Video S1, a layer of clay as well as HM molecules consisting of 100 units were constructed. The amount of interaction energy ($E_{Interaction}$) between sepiolite and HM was calculated by the simulation to be −3823.1 kcal/mol, which indicates that HM molecules were attracted to the sepiolite surface. This result is consistent with the Zeta analysis. Meanwhile, it can be found that the HM molecular chain was rapidly adsorbed to the surface of sepiolite within 200 ps, which proves that HM molecules can form nanoparticles with sepiolite rapidly. Further analysis revealed that a large number of intramolecular hydrogen bonds consisting of hydroxyl groups and N–H were presented inside HM, which further confirmed the self-assembly mechanism of HM, as shown in Fig. 2e. The hydroxyl and alkyl groups on HM molecules can form a hydrogen bond with Si–O groups on the surface of sepiolite, which is consistent with the FT-IR analysis (Fig. 2f). These results suggest that HM can be assembled to the clay surface by electrostatic interactions and hydrogen bonding, while intermolecular hydrogen bonding exists on HM itself to obtain a tighter polymer layer. Accordingly, it is not difficult to postulate that a larger nanoparticle size can be achieved at a lower LAP concentration since excessive HM which harbored a positive charge completely shields the negative charge of LAP. In contrast, a higher amount of LAP reduces the number of adsorbable HM chains, which results in smaller nanoparticles (Fig. 2g) [35].

Together, the above data suggest that LAP interacts with and is coated by HM through electrostatic interaction and hydrogen bonding, thereby constituting the interior structure of HML nanocomposites.

3.2. Preparation and characterization of HML nanocomposites hydrogels

The nanocomposites are in a fluid state and can be easily injected using a 23 G needle. After UV irradiation for 2 min, the nanocomposites were crosslinked into a hydrogel and lost fluidity. The nanocomposites were also mouldable, which could be applied to fill different kinds of defects. For instance, the nanocomposites can fill complex shapes and form hydrogels *in situ* (Fig. 3a). The rheological analysis further confirmed that the HM_2 and HM_2L_5 nanocomposite has liquid property (G'<G″), while the addition of LAP improved the viscosity and modulus

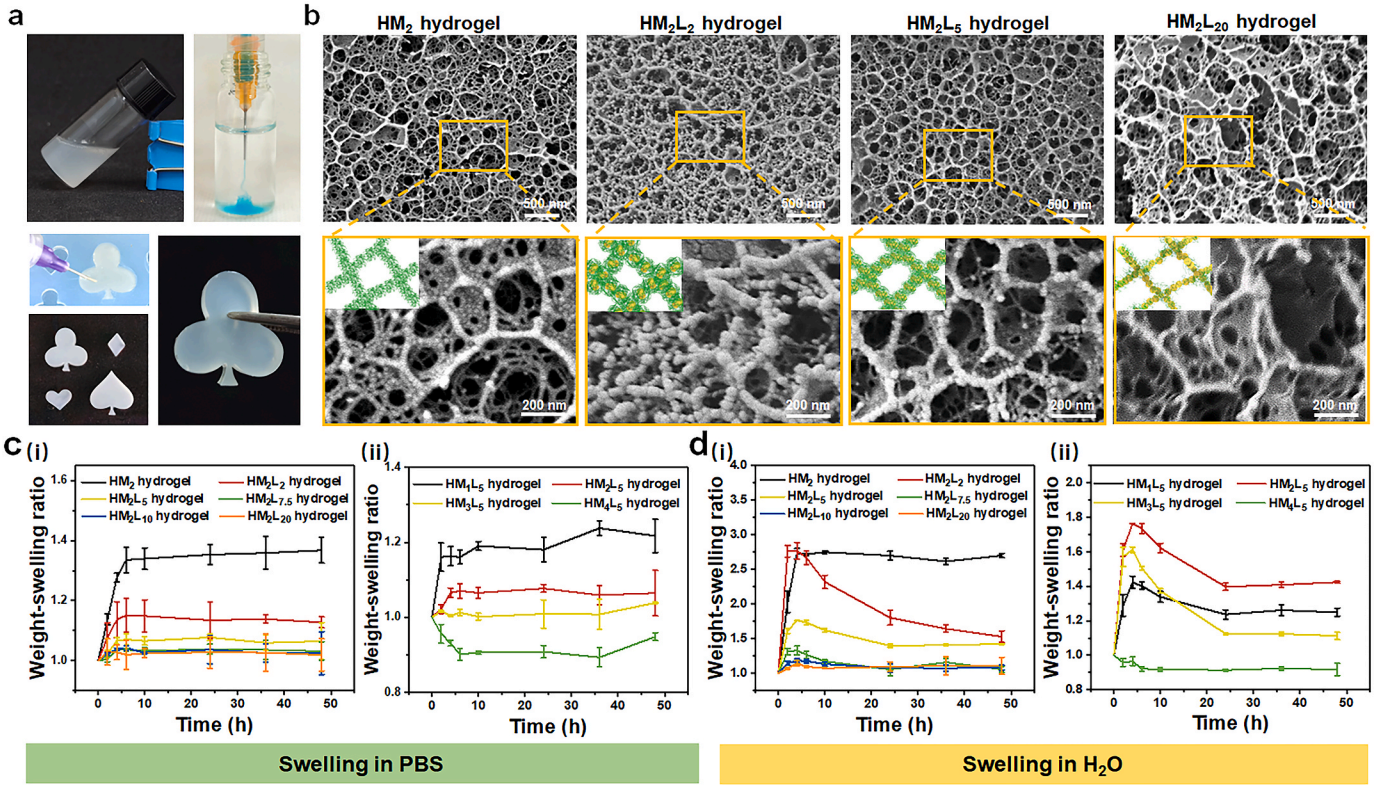

Fig. 3. Microstructural characteristics and swelling behaviors of the HML hydrogels. a) Photographs of the HM_2L_5 nanocomposite showing its fluidity, injectability, and various shapes after *in situ* crosslinking in moulds. b) Cryo-SEM images of different nanocomposite hydrogels. (Inset: schematic illustration of the possible fibrillar network). The weight-swelling dynamics of different nanocomposite hydrogels in c) PBS and d) water, with different (i) LAP concentrations and (ii) DS_{MA}.

(Figs. S4a–b). These results suggest that the HM_2 and HM_2L_5 hydrogel are injectable and can be utilized as *in situ* forming materials. Cryo-SEM allowed for the imaging of hydrogel microtopography by removing the liquid phase via sublimation, which can observe the real morphology of hydrogels. The internal morphology of hydrogels (HM_2, HM_2L_2, HM_2L_5, and HM_2L_{20}) was visualized by cryo-SEM, and the results are presented in Fig. 3b. All hydrogels showed a high surface area and 3D porous nanostructure, in which pores were in the range of 0–750 nm (Figs. S5a–b). The HM_2 hydrogel consisted of interconnected nanofibers with a diameter of ~30 nm. Meanwhile, the nanofibers appeared to be assembled from granular nanoparticles. Sizes of these nanoparticles as determined by cryo-SEM were larger than that of those nanoparticles measured by SEM; this is likely due to the contraction/collapse of samples during SEM sample preparation. The diameter of the nanofibers increased from 30 nm to 50 nm with the addition of LAP (2 mg/mL), while there was uniformly crosslinked and showed collagen fibril-like nanostructure. In HM_2L_5 hydrogel, the nanofibers displayed the assembly of smaller granular particles, and their diameter decreased to 40 nm. At a high concentration of the HM_2L_{20} hydrogel, they formed large-area thin films with interconnected nanofibers rather than agglomerated granular particles. In agreement with the aforementioned nanocomposite results, nanoparticles were found to distribute in the hydrogels, while the size of nanoparticles and the corresponding nanofibers decreased or even disappeared and formed into flakes with the increasing LAP concentration. It is suggested that after irradiation, the nanoparticles in nanocomposites were crosslinked to form nanofibers and 3D crosslinked networks. Meanwhile, the addition of excessive LAP resulted in a reduction in the amount of HM on its surface, leading to a lamellar cross-linked network.

Since the *in situ*-formed hydrogels are mainly used to fill defects for long-term applications, appropriate anti-swelling properties are necessary to prevent excessive swelling of the hydrogel from squeezing the wound or breaking the hydrogel. To demonstrate the swelling dynamics of nanocomposite hydrogels in different solutions (PBS, DMEM, and H_2O), the weight-swelling ratio at various times was measured (Fig. 3c, d and Fig. S6). In PBS, the weight-swelling ratio of all hydrogels showed a tendency to rise first and then reach an equilibrium, except for HM_4L_5 hydrogel (Fig. 3c). The LAP concentrations and the DS_{MA} of hydrogels were both negatively correlated with its equilibrium weight-swelling ratio (Q_m). The Q_m of soft and tough HM_2L_5 hydrogel in PBS was 1.07, in particular. In Fig. S7, HM_2 hydrogel and HM_2L_5 hydrogel immersed in PBS exhibited slight volume swelling and remained stable within 48 h. As previously described, hydrogels with a Q_m of less than 1.5 can be defined as anti-swelling [36]. Meanwhile, the Q_m and swelling dynamics of hydrogels in DMEM were consistent with those in PBS (Fig. S6), suggesting that the hydrogels in saline solution and physiological environment exhibited wonderful anti-swelling ability. However, hydrogels placed in the water displayed a higher Q_m than that in PBS, which can be explained by the Flory-Rehner theory that the swelling ratio of hydrogels decreases with an increasing salt concentration in the external solution [37]. Almost all hydrogels in water showed an increasing Q_m first and then reached equilibrium (Fig. 3d), which can be attributed to the competition between the polymer-water interaction force and the elastic retractive force [36]. Interestingly, the HM_4L_5 hydrogel with the highest DS_{MA} displayed shrinkage in each solution including PBS, DMEM, and H_2O. Additionally, all hydrogels show stability in different environments. Three possible reasons exist to support these findings: (i) The amphiphilicity of HM weakens the interaction between polymer chains and water molecules; (ii) With the increasing addition of LAP, the physical crosslinking density increases thereby limiting the extension of HM chains; (iii) The chemical cross-linking between/within nanoparticles increased the elastic retractive force of the crosslinking network, and the elastic force endeavored to resist the decrease of the configurational entropy caused by the network expansion through retracting the network chain.

Preservation and retention of the activity of therapeutic proteins at delivery sites are fundamental for *in vivo* experiments and regenerative medicine [38]. Therefore, the drug delivery performance of nanocomposite hydrogels was tested for 7 d using BSA as a representative loaded biomolecule (Fig. S8). All hydrogels showed initial fast release in 2 h and then reached an equilibrium state after 48 h, which remained constant during the rest of the incubation period. Compared with HM_2 hydrogel, BSA release from the nanocomposite hydrogels was slower. After 7 days, the ratios of released BSA from HM_2L_2 hydrogel, HM_2L_5 hydrogel, $HM_2L_{7.5}$ hydrogel, HM_2L_{10} hydrogel, and HM_2L_{20} hydrogel were 89.7%, 72.8%, 78.3%, 68%, and 16.2%, respectively. It is reported that LAP could promote the retention of BSA in a dose-dependent manner [38,39], we then inferred that the BSA adsorption to the LAP surface enhanced the retention of BSA inside the hydrogel. Interestingly, although an increase in DS_{MA} enhanced the crosslinking density in the nanocomposite hydrogels, it led to faster release of BSA and decreased retention times, likely due to the volume shrinkage of the hydrogels.

Taken together, it is of significance that the nanocomposite hydrogels possess excellent anti-swelling properties and drug retention ability, making them promising scaffolds for a variety of tissue engineering applications.

3.3. Mechanical properties of the nanocomposite hydrogels

The mechanical properties of hydrogels are critical in tissue engineering and regenerative medicine applications. Thus, a series of mechanical tests were performed for the newly developed hydrogels. Of note, all hydrogels with different LAP concentrations displayed high ductility (>65%), as measured by confined compression tests (Fig. 4a and Fig. S9a). Next, the compression modulus and compressive strength of hydrogels were calculated based on the stress-strain curve. As shown in Fig. 4b and Fig. S9b, the compressive modulus of nanocomposite hydrogels increased with the increase of both LAP concentration and chemical cross-linking degree (DS_{MA}, UV irradiation time), which ranged between 3.5 and 40 kPa. The compressive modulus of hydrogels depends on their configurational degrees of freedom of the polymer chain [40]. The increased LAP content and chemical cross-linking restrict the freedom of HM chains to varying degrees, further causing an enhancement of the compression modulus. Moreover, appropriate crosslinking could elevate the compression strength, while an excessively high crosslinking density on the other hand could result in a stiffer and more brittle network [41] (Fig. 4c and Fig. S9c). Among these hydrogels, soft and tough HM_2L_5 hydrogel exhibited the optimal characteristics, which could be efficiently prepared (2 min), sustained large strain (76%), and showed low compressive modulus (7.3 kPa) and the highest compressive strength (709.9 kPa).

The optimal hydrogels were subsequently subjected to another loading-unloading cycle test, which indicates energy dissipation during compression. We observed that the HM_2L_5 hydrogel exhibited dramatic hysteresis loops at different maximum strains (60%, 65%, 70%), indicating that this cross-linked network provided effective energy dissipation capability for the hydrogels [10] (Fig. S9d). With the maximum strain increasing from 60% to 65% and 70%, the dissipated energy per unit volume of hydrogels were 3.04, 5.13, and 10.58 kJ m^{-3} in the first cycle, respectively, suggesting that the larger cross-linking networks were destroyed to dissipate energy at the higher strains (Fig. S9e). However, the dissipation energy was decreased in the subsequent cycles, which is due to the breakage of the irreversible chemical bond. Interestingly, the HM_2L_5 hydrogel can recover to its original height after five cycles, showing 90.01%, 87.50%, and 73.00% reversible stress retention at 60%, 65%, and 70% strain, respectively, confirming excellent fatigue resistance (Figs. S9d and f). It is noted that HM_2L_5 hydrogel showed high toughness and flexibility, which could be folded and knotted, and even swung back and forth (Fig. 4d and Video S2). To investigate the effect of LAP on the mechanical properties of hydrogels, the rheological behaviors of HM_2 hydrogel and HM_2L_5 hydrogel were further evaluated (Fig. 4e and Fig. S10). Both samples here presented the typical

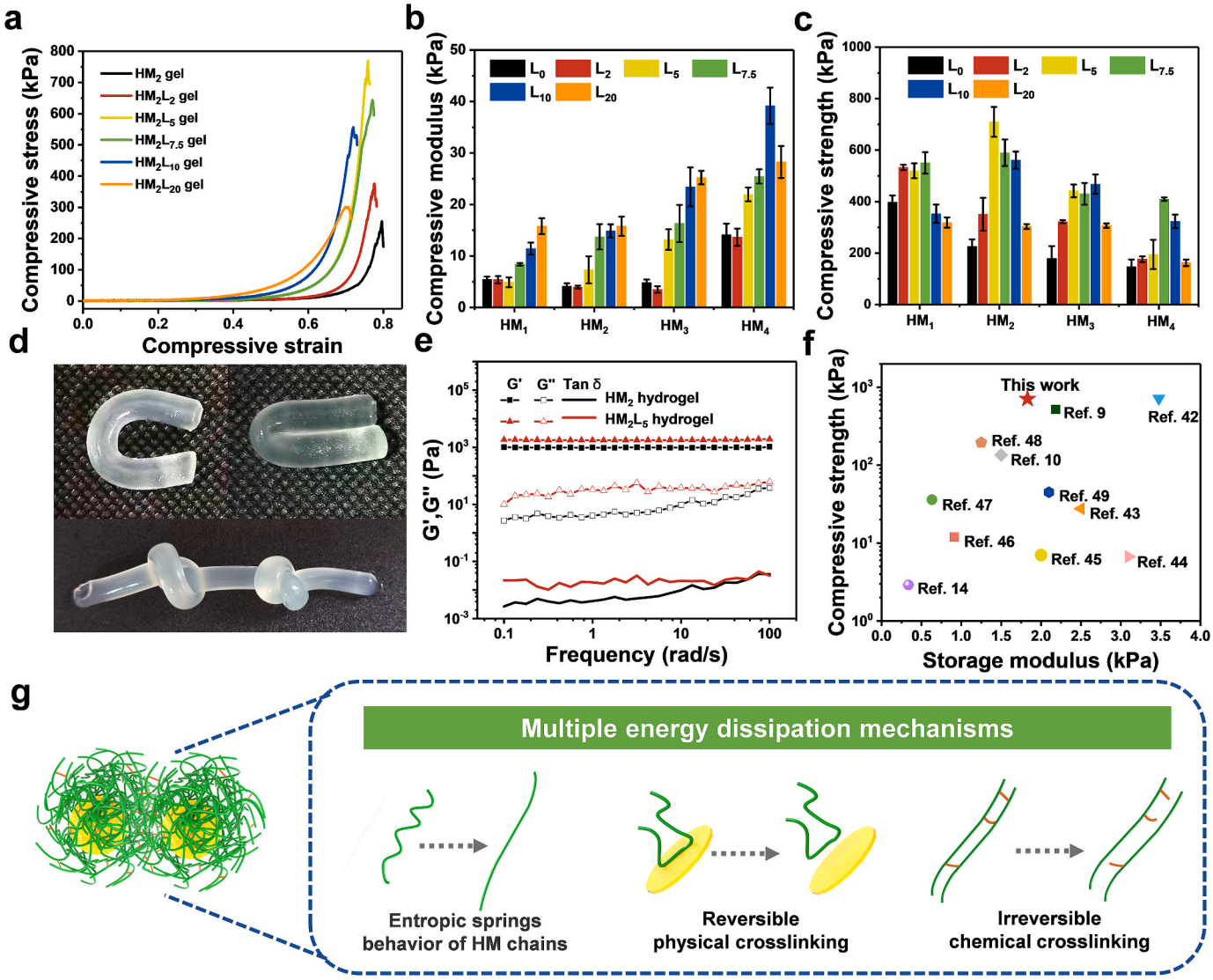

Fig. 4. Mechanical characterization of the nanocomposite hydrogels. a) Representative compressive stress-strain curves of the HM_2 hydrogels reinforced with various concentrations of LAP. b) Compressive modulus and c) compressive strength of different hydrogels fabricated by different concentrations of LAP (L_x, x = 0, 2, 5, 7.5, 10, and 20 mg/mL) and HM of different DS_{MA} (HM_1, HM_2, HM_3, and HM_4). d) Representative images of the HM_2L_5 hydrogel showing its high flexibility. e) Frequency sweeps rheological measurements of HM_2 hydrogel and HM_2L_5 hydrogel. f) Compressive strength versus storage modulus chart comparing the mechanical performance of HM_2L_5 hydrogel developed in this work and injectable, soft, and natural polymer-derived hydrogels reported previously [9,10,14,42–49]. g) Schematic illustration of the possible energy dissipation mechanism of HM_2L_5 hydrogel.

viscoelastic behavior of hydrogel phases (G' > G″) and slight frequency-dependent moduli, while the G′, G″, and the yield stress of HM_2L_5 hydrogel were higher than HM_2 hydrogel. It indicates that there were some reversible bonds in the hydrogels, and the addition of LAP greatly improved the mechanical properties of the hydrogels. Moreover, the G' of HM_2 hydrogel and HM_2L_5 hydrogel were only 1.04 kPa and 1.83 kPa, respectively, confirming their softness.

Based on the above results, the soft and tough properties of HM_2L_5 hydrogel could be attributed to the multiple mechanical energy dissipation mechanisms in the nanofibrillar network, including the entropic springs behavior of HM chains, reversible physical crosslinking between HM and LAP, and irreversible chemical crosslinking (Fig. 4g). As the hydrogel deforms, the HM chains shift from coiled coils to a taut state, while the physical HM-LAP crosslinking is disrupted to dissipate energy, and when the stress is further increased, some of the chemical crosslinking between the HMs is disrupted to dissipate energy. Owing to the multiple mechanical energy dissipation mechanisms, the mechanical stability of HM_2L_5 hydrogel was higher than that of most previously developed injectable, soft, natural polymer-derived hydrogels (Fig. 4f). Thus, these results demonstrated the low modulus, excellent compressive strength, and fatigue resistance of HM_2L_5 hydrogel, which are highly desirable mechanical properties for soft tissue regeneration.

3.4. 3D printing performance of the nanocomposite microgels

Since 3D printing can be designed to create personalized materials for different tissues and needs, it has attracted considerable attention in the biomedical field, such as personalized wound dressings [50,51]. However, HM_2L_5 hydrogel lacks printability and potential for advanced biofabrication. Recently, microgels have been used in 3D printing to achieve complex custom shapes [52,53]. Therefore, the nanocomposite microgels were prepared (Fig. 5a). The nanocomposite microgels were fabricated by pre-crosslinking for 0–60 s and sieving twice, according to the injectability analysis of microgels with different treatments (Fig. S11a). The obtained microgels were opaque, microporous, and mouldable (Fig. S11b). By the photo-crosslinking ability of

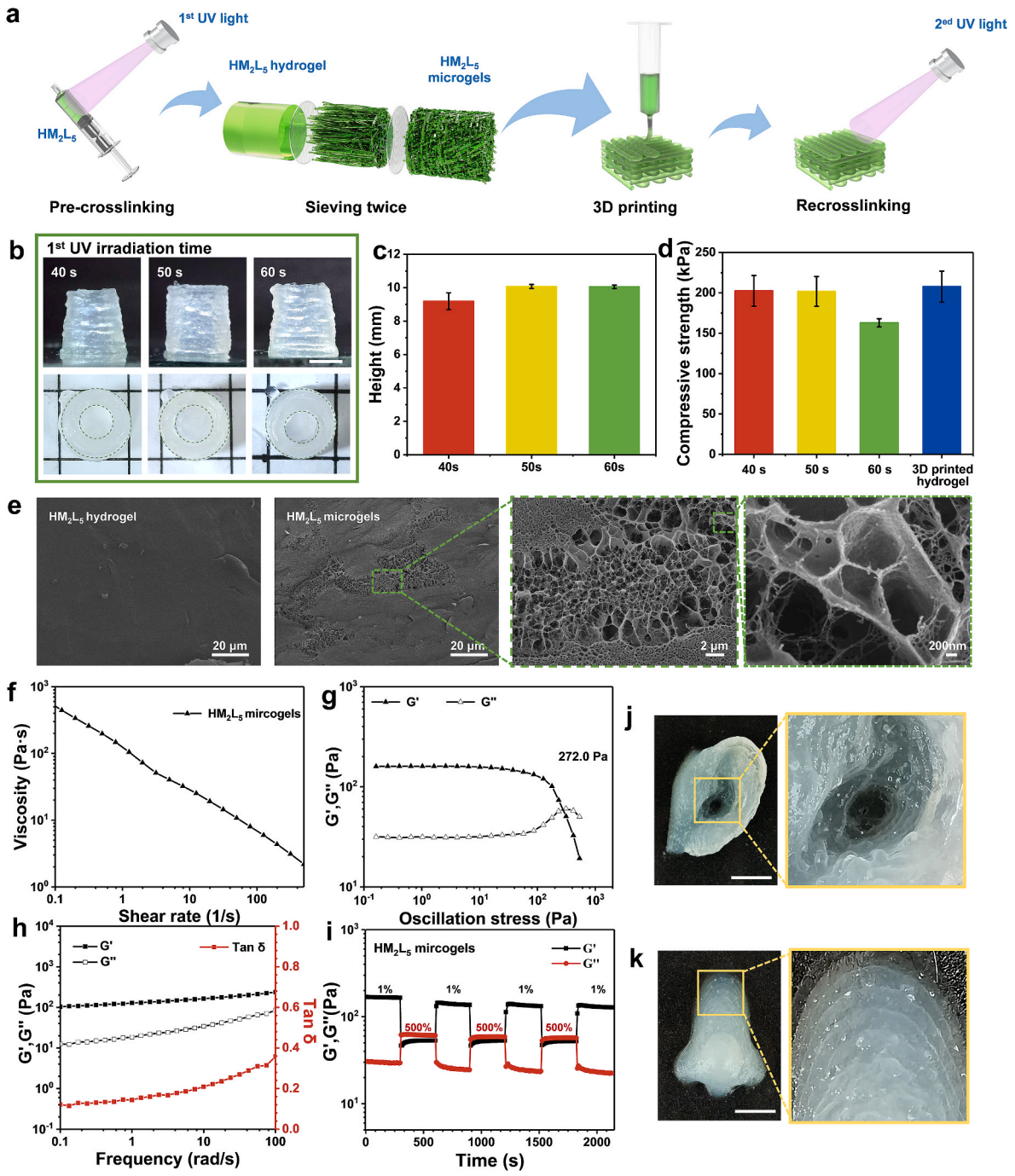

Fig. 5. Preparation of microgels and their application in 3D printing. a) Schematic illustration of microgel preparation and subsequent 3D printing. b) Representative images (scale bar = 0.5 cm) and c) quantitative analysis of printability of microgels prepared with different pre-crosslinking time. d) Compressive strength of hydrogels made from microgels prepared with different pre-crosslinking time (40 s, 50 s, 60 s) and the 3D printed hydrogel made from microgels (50 s), while keeping the total crosslinking time 2 min. e) Cryo-SEM images of HM_2L_5 hydrogel and HM_2L_5 microgels. f) Shear rate sweeps and g) amplitude sweeps of HM_2L_5 microgels. h) Frequency sweeps of HM_2L_5 microgel. i) Step strain sweeps of the HM_2L_5 microgels (1 Hz, 1%, and 500% strain). Each strain interval was kept as 300 s. j) Ear-shaped and k) nose-shaped constructs 3D printed from the HM_2L_5 microgel. Scale bar = 1 cm.

nanoparticles and microgels, the HM_2L_5 microgels could be handled and manipulated with forceps after secondary crosslinking (Fig. S11c). In Fig. 5b–d, the greater the degree of pre-crosslinking, the higher the shape fidelity of the resulting microgels, but the lower the mechanical strength of the final hydrogel. Thus, the UV irradiation of 50 s and two rounds of sieving was chosen as the condition for the preparation of the microgels. Of note, the mechanical strength of these microporous hydrogels was reduced when compared to the HM_2L_5 hydrogel. This can be explained by the fact that the two rounds of sieving break part of the crosslinking network of the hydrogel. Nevertheless, the 3D printed hydrogel fabricated by these conditions maintained good compressive strength (207.8 kPa, Fig. 5d). As shown in Fig. 5e, different from HM_2L_5 hydrogel, HM_2L_5 microgels presented micron-scale localized porous structure, which indicates the formation of micropores within the hydrogels.

The rheological properties of HM_2L_5 microgels were investigated. As shown in Fig. 5f, the HM_2L_5 microgels showed a typical shear thinning behavior, which was previously demonstrated to be critical for 3D

printing. The yield stress of the HM_2L_5 microgels was 272 Pa, leading to high shape fidelity (Fig. 5g). Frequency sweep results showed that the HM_2L_5 microgels had frequency-dependent moduli and gel-like behavior within the entire frequency range, attributed to the physical network based on hydrogen bonding (Fig. 5h). Moreover, the shear recovery behavior of HM_2L_5 microgels was investigated by imposing alternating high and low shear strain cycles (Fig. 5i). The results showed that the HM_2L_5 microgels demonstrated a high shear recovery rate of 80.4% after four cycles. This excellent recoverability renders HM_2L_5 microgels a promising candidate for high-resolution 3D printing applications.

Next, we sought to explore the potential of microgels to fabricate large complex 3D constructs. As expected, we were able to print several biologically relevant structures including the ear and nose with the above microgels (Fig. 5j and k). A human ear of 30 × 24 × 20 mm and a nose of 30 × 26 × 6.5 mm were printed, implying the potential of these microgels to create macro-sized scaffolds. These printed structures were stable enough, even after stacking 52 layers along the z-direction. These

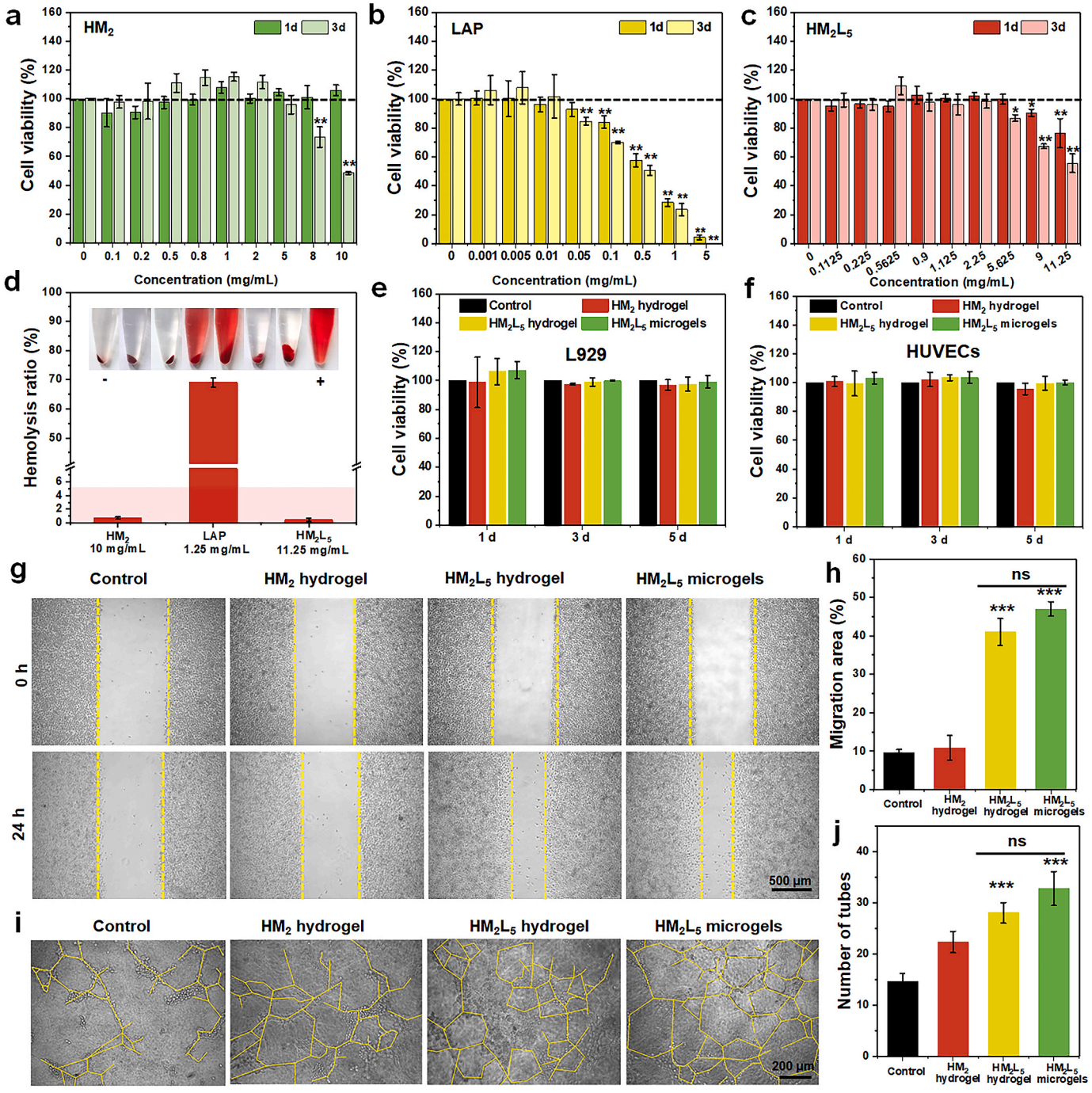

Fig. 6. Viability of hMSCs cultured in a) HM_2, b) LAP, and c) HM_2L_5 nanocomposite solutions at different concentrations for 24 h and 72 h (n = 6, mean ± SD). d) *In vitro* hemolytic activity of HM_2, LAP, and HM_2L_5 nanocomposite. (Inset: representative images from hemolytic activity assay of the sample and controls) (n = 6, mean ± SD). Viability of e) L929 cells and f) HUVECs after co-culturing with different hydrogels for 1, 3, and 5 d. g) Representative images of L929 cells before (0 h) and after culturing them in a hydrogel-conditioned medium for 24 h. h) The migration area rate after 24 h of culture in hydrogel-conditioned medium. i) Representative images showing the effects of different hydrogels on the tube formation by HUVECs. j) Number of tubes formed by HUVECs after different treatments. ***$p < 0.01$, **$p < 0.01$, *$p < 0.05$ (one-way ANOVA).

results indicate that the HM_2L_5 hydrogel can form 3D printable ink according to the processing strategy, which has high shape fidelity and can be applied for constructing large complex structures, indicating its potential in the application of personalized tissue engineering. To further explore the potentials of the HM_2L_5 microgels obtained by this processing strategy, its biological properties were examined in follow-up experiments.

3.5. *In vitro biocompatibility and biological efficiency of the nanocomposite hydrogels*

Next, we sought to explore the biological properties of the above hydrogels. Since *in situ* formed hydrogels first contact cell/defect site as a precursor solution, then the biocompatibility of precursors was firstly evaluated. The cytotoxicity of HM_2 solution (0.1–10 mg/mL), LAP solution (0.001–5.0 mg/mL), and HM_2L_5 solution (0.1125–11.25 mg/mL) was examined using human bone marrow mesenchymal stem cells (hMSCs). Notably, hMSCs cultured in 0.1–5 mg/mL HM_2 demonstrated high cell viability (Fig. 6a). Similar to the previous reports [54,55], promotingcell proliferation was found upon the treatment with LAP at relative low concentrations (0.001–0.01 mg/mL) in 3 d, whereas, a higher concentration of LAP (more than 0.05 mg/mL) resulted in a significant suppression of hMSCs viability (Fig. 6b). The toxicity at a higher dose of LAP can be explained by the LAP internalization which might restrict the celluar functionality and/or the formation of aggregates with the media proteins that are toxic to the cells [54]. Interestingly, the HM_2L_5 nanocomposite (total concentration of 0.1125–2.25 mg/mL) showed no cytotoxicity on the hMSCs viability, presumably, it can counteract the cytotoxicity of pure LAP at the same concentrations (Fig. 6c). Together, we speculate that the nanoparticles, formed by LAP coating with HM_2, had higher biocompatibility than LAP alone, possibly as a result of an increase in the nanoparticle size and hence decreased internalization by the cells.

Furthermore, the hemocompatibility assessment revealed that the HM_2 and HM_2L_5 displayed excellent blood biocompatibility with hemolysis values lower than 5%, while the LAP group showed high hemolysis ratio, an issue not sufficiently addressed in previous studies (Fig. 6d).

Additionally, the biocompatibility of HM_2 hydrogel and HM_2L_5 hydrogel were determined by CCK-8 assay and lived/dead staining (Fig. 6e,f, and Fig. S12). All treatments showed no significant effect on the cell viability of L929, HEVECs, and hMSCs. Furthermore, the potential toxicity of the HM_2L_5 hydrogel was evaluated *in vivo*. Compared with the control, the organs (heart, liver, spleen, lung, and kidney) of the mice treated with HM_2L_5 hydrogel showed no obvious changes (Fig. S13). The results collectively suggest that the nanocomposites before or after photo-crosslinking display good biocompatibility and are safety for tissue engineering applications.

During the process of skin wound healing, cell migration is an important part of wound contraction and later healing. Scratch assay was used to evaluate the effects of different nanocomposites on L929 dermal fibroblasts *in vitro* (Fig. 6g and h). Of note, the HM_2L_5 hydrogel and HM_2L_5 microgel groups showed a faster cell migration than that of the control (LAP untreated) group. In addition, the HM_2L_5 hydrogel and HM_2L_5 microgel groups were found to significantly increase the amount of capillary tube formation in HUVECs after 4 h (Fig. 6i and j). These findings are supported by a recent report that magnesium and silicon ions released from the LAP promote cell migration [56,57].

3.6. *The application of HM_2L_5 hydrogel for promoting wound healing*

The degradation properties of hydrogels both *in vitro* and in *vivo* are critical for biomaterials and tissue engineering. Herein, we found that all hydrogel exhibited degradable characteristics in the lysozyme solution (Fig. S14). Of note, LAP addition could delay the degradation of hydrogel, while the introduction of micropores compromised the delayed effects. Nevertheless, due to the more complex environment in the body, all hydrogels degraded completely within 7 d after subcutaneous implantation (Fig. 7a). Additionaly, we observed that the hydrogel treatment caused a minor immune response (neutrophil infiltration) at 7 d but the response was resolved at day 14 as essessed by the H&E staining (Fig. S15), indicating a favorable outcome in biodegradability and inflammatory response during tissue healing.

Skin is an extremely important soft tissue, and its repair has attracted numerous concerns. From the above results, it is clear that HM_2L_5 hydrogel and microgels have excellent biocompatible, injectability, low stiffness, sufficient mechanical strength, drug delivery, and anti-swelling properties, which rendered them great potential for promoting wound healing. Compared to the existing commercial wound dressings, HM_2L_5 hydrogel and microgels can be filled into the irregular shape of wounds, and/or personalized with different shapes, pore structures, and even with pro-healing agents. Additionally, increasing evidence has suggested that HCS and LAP, either alone or in combination with other factors, exhibit excellent ability to promote wound healing [24,58]. However, the effect of HM_2L_5 hydrogel on wound tissue regeneration has yet to be studied. Therefore, a full-thickness skin defect model was established as previously described [59]. Of note, treatment with HM_2L_5 microgels and HM_2L_5 hydrogel remarkably accelerated the wound closure by day 3 and continued in the following days when compared to the control and HM_2 hydrogel (Fig. 7b and c). Simultaneously, more new granulation tissue appeared in the HM_2L_5 hydrogel and HM_2L_5 microgels group on day 7 (Fig. S16). The H&E staining on day 11 revealed that the wound of the HM_2L_5 hydrogel and HM_2L_5 microgels group were completely healed, with a strong connection between the epidermis and dermis (Fig. 7d). In contrast, a large ulcer and granulation tissue infiltrated by inflammatory cells remained in the control and HM_2 hydrogel group. Similar results were confirmed by Masson staining, in which the HM_2L_5 hydrogel and HM_2L_5 microgels group displayed the highest density of collagen and substantial amounts of neovascularization, compared to the other two groups (Fig. 7d). To further determine the maturation of neovascularization, the 11-day samples were subjected to immunofluorescence staining using antibodies against CD31 and α-SMA, which are two important markers for vascular endothelial cells and pericytes, respectively. As expected, more mature vessels as labeled by the CD31 (red) and α-SMA (green) were found in the HM_2L_5 hydrogel and HM_2L_5 microgels group compared to the control group (Fig. 7e, Fig. S17). All these results suggest that the pro-healing effect of the hydrogel was better after the addition of LAP, highlighting the importance role of LAP in amplifying the hydrogel's pro-healing properties. Collectively, our data highlight the promising role of the biomimetic nanofibrillar hydrogels and soft hydrogels in promoting wound healing by facilitating the fibroblasts' migration and the angiogenesis (Fig. 7f). These results also indicate that the microgel processing would not damage the original wound healing ability of the HM_2L_5 hydrogel, rather, they exhibit great potential in personalized wound dressings.

4. Conclusion

In summary, by crosslinking self-assembled HML nanoparticles, we have developed a collagen fibril-like injectable hydrogel with low stiffness, high compressive strength, anti-swelling properties, sustained drug release ability, and biodegradability. To fabricate this novel hydrogel, HM and LAP first self-assembled, by electrostatic and hydrogen bonding action, into nanoparticles, which further bonded with each other by photo-crosslinking to form the collagen fibril-like network. This network consisted of highly entangled HM molecular chains, reversible physical polymer-clay cross-links, and robust chemical cross-links, thus allowing efficient stress dissipation across the network within a soft and flexible hydrogel. Due to the synergistic effects of the restricted molecular chain movement caused by self-assembly and the amphipathicity of HM, the nanocomposite hydrogels

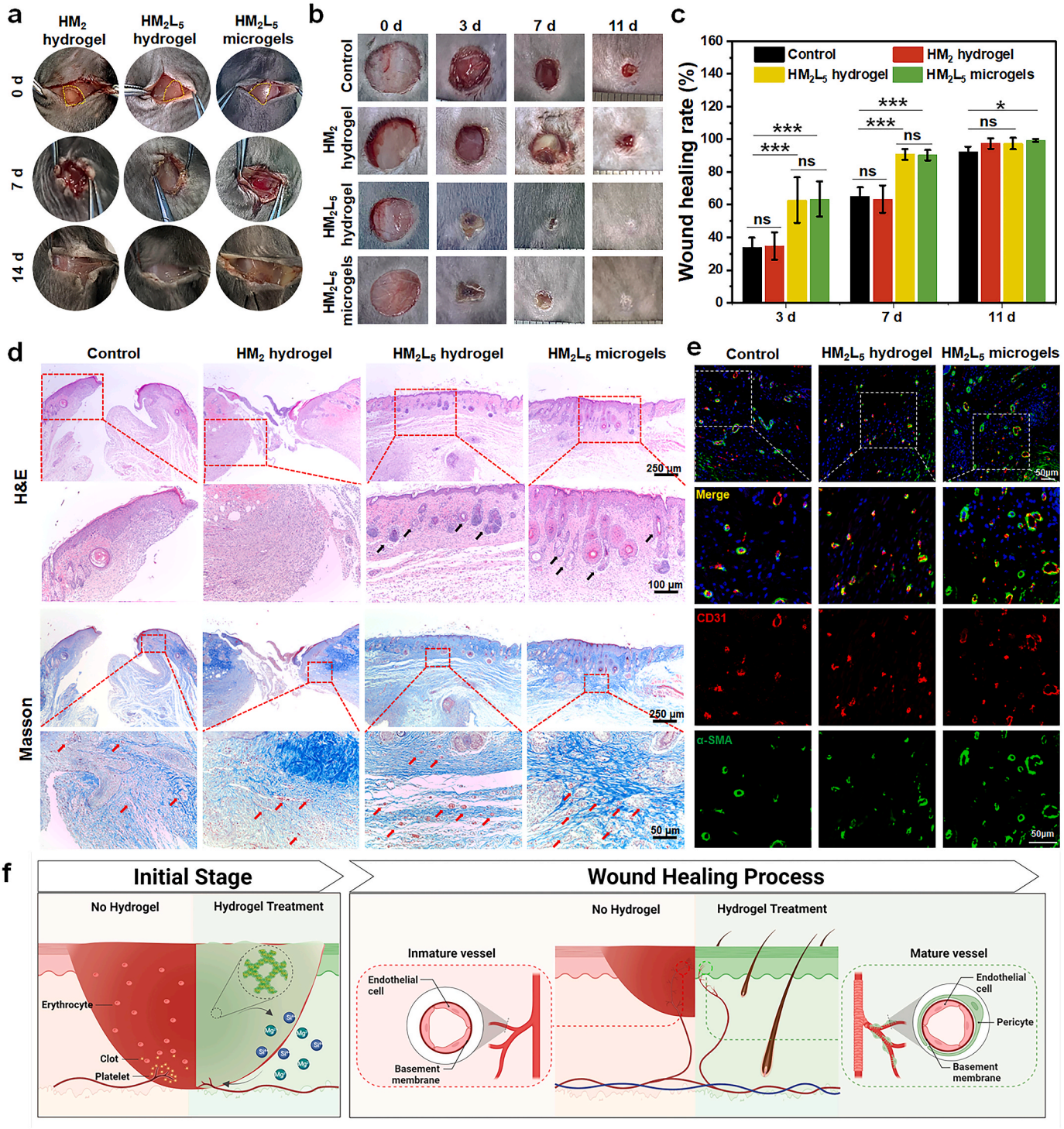

Fig. 7. a) Representative images of the subcutaneously implanted hydrogels on 0 d, 7 d, and 14 d (n = 3). b) Representative images of the temporal development of healing wounds from day 0 to day 11 with the use of different hydrogels. c) Quantification of wound healing rate at different healing times. d) Histological evaluation of the wound section on the 11th day for each group by the H&E and Masson staining. The black arrows point to appendages, hair follicles, and sebaceous glands, and the red arrows define blood vessels. (n = 5) e) Representative immunofluorescence staining images of the wound section on the 11th day for each group. f) Schematic illustration of the wound healing process with and without hydrogel treatment. Mean ± SD, *p < 0.05, **p < 0.01, ***p < 0.001 (one-way ANOVA).

exhibited remarkable anti-swelling behavior in different solvents. Additionally, the nanocomposite hydrogels could be processed into 3D printable microgels with high shape fidelity, making them promising bioinks for large-size and complex constructs. Furthermore, the HM_2L_5 hydrogel and microgels demonstrate high biocompatibility *in vitro*, as well as excellent wound healing ability and biodegradability *in vivo*. These results collectively demonstrated the promising potential of these novel biomimetic hydrogels in various tissue engineering applications such as wound dressing. This work provides a versatile strategy for the development of biomimetic nanofibrillar soft hydrogels for long-term biomedical applications.

CRediT authorship contribution statement

Shanshan Li: Conceptualization, Methodology, Validation, Investigation, Data curation, Visualization, Writing – original draft, Writing – review & editing. **Xiaoyun Li:** Conceptualization, Resources, Investigation, Supervision, Writing – review & editing. **Yidi Xu:** Methodology, Validation, Investigation, Data curation, Visualization, Writing – original draft, Writing – review & editing. **Chaoran Fan:** Methodology, Validation. **Zhong Alan Li:** Supervision, Writing – review & editing. **Lu Zheng:** Investigation, Data curation. **Bichong Luo:** Data curation, Visualization. **Zhi-Peng Li:** Validation. **Baofeng Lin:** Methodology, Validation. **Zhen-Gang Zha:** Supervision, Funding acquisition. **Huan-Tian Zhang:** Conceptualization, Visualization, Supervision, Project administration, Funding acquisition, Writing – review & editing. **Xiaoying Wang:** Conceptualization, Visualization, Supervision, Project administration, Funding acquisition, Writing – review & editing.

Declaration of competing interest

The authors declare that they have no known competing financial interests or personal relationships that could have appeared to influence the work reported in this paper.

Acknowledgements

This work was financially supported in part by the Guangdong Basic and Applied Basic Research Foundation (Nos. 2020B1515120038 and 2021A1515012154), the Fundamental Research Funds for the Central Universities (No. 2022ZYGXZR105), the National Natural Science Foundation of China (Nos. 82072470 and 81871809), the State Key Laboratory of Pulp and Paper Engineering (No. 2022C02). We would like to thank Prof. Min-Feng Chen for technical assistance. The simulation was supported by the High-performance Computing Platform of Guangxi University. Zhong Alan Li acknowledges the support from the Vice-Chancellor Early Career Professorship Scheme of The Chinese University of Hong Kong.

Appendix A. Supplementary data

Supplementary data to this article can be found online at https://doi.org/10.1016/j.bioactmat.2023.09.012.

References

[1] Y.F. Ma, M. Lin, G.Y. Huang, Y.H. Li, S.Q. Wang, G.Q. Bai, T.J. Lu, F. Xu, 3D spatiotemporal mechanical microenvironment: a hydrogel-based Platform for guiding stem cell fate, Adv. Mater. 30 (49) (2018), 1705911, https://doi.org/10.1002/adma.201705911.

[2] L.A.S. Callahan, A.M. Ganios, E.P. Childers, S.D. Weiner, M.L. Becker, Primary human chondrocyte extracellular matrix formation and phenotype maintenance using RGD-derivatized PEGDM hydrogels possessing a continuous Young's modulus gradient, Acta Biomater. 9 (4) (2013) 6095–6104, https://doi.org/10.1016/j.actbio.2012.12.028.

[3] S. Lee, A.E. Stanton, X.M. Tong, F. Yang, Hydrogels with enhanced protein conjugation efficiency reveal stiffness-induced YAP localization in stem cells depends on biochemical cues, Biomaterials 202 (2019) 26–34.

[4] A.J. Engler, S. Sen, H.L. Sweeney, D.E. Discher, Matrix elasticity directs stem cell lineage specification, Cell 126 (4) (2006) 677–689, https://doi.org/10.1016/j.cell.2006.06.044.

[5] A.K. Whitehead, H.H. Barnett, M.E. Caldorera-Moore, J.J. Newman, Poly (ethylene glycol) hydrogel elasticity influences human mesenchymal stem cell behavior, Regen Biomater 5 (3) (2018) 167–175, https://doi.org/10.1093/rb/rby008.

[6] T.H. Kim, D.B. An, S.H. Oh, M.K. Kang, H.H. Song, J.H. Lee, Creating stiffness gradient polyvinyl alcohol hydrogel using a simple gradual freezing-thawing method to investigate stem cell differentiation behaviors, Biomaterials 40 (2015) 51–60, j.biomaterials.2014.11.017.

[7] B. Trappmann, J.E. Gautrot, J.T. Connelly, D.G.T. Strange, Y. Li, M.L. Oyen, M.A. C. Stuart, H. Boehm, B.J. Li, V. Vogel, J.P. Spatz, F.M. Watt, W.T.S. Huck, Extracellular-matrix tethering regulates stem-cell fate, Nat. Mater. 11 (7) (2012) 642–649, https://doi.org/10.1038/nmat3339.

[8] E. Hui, K.I. Girneno, G. Guan, S.R. Caliari, Spatiotemporal control of viscoelasticity in phototunable hyaluronic acid hydrogels, Biomacromolecules 20 (11) (2019) 4126–4134, https://doi.org/10.1021/acs.biomac.9b00965.

[9] S. Wang, J.H. Chi, Z.W. Jiang, H.W. Hu, C.Z. Yang, W.S. Liu, B.Q. Han, A self-healing and injectable hydrogel based on water-soluble chitosan and hyaluronic acid for vitreous substitute, Carbohydr. Polym. 256 (2021), 117519, https://doi.org/10.1016/j.carbpol.2020.117519.

[10] K. Chen, Z.H. Wu, Y.T. Liu, Y. Yuan, C.S. Liu, Injectable double-crosslinked adhesive hydrogels with high mechanical resilience and effective energy dissipation for joint wound treatment, Adv. Funct. Mater. 32 (12) (2022), 2109687, https://doi.org/10.1002/adfm.202109687.

[11] Z.M. Liu, B.F. Zhao, L.C. Zhang, S.T. Qian, J.Y. Mao, L.Y. Cheng, X.Y. Mao, Z. W. Cai, Y.G. Zhang, W.G. Cui, X.M. Sun, Modulated integrin signaling receptors of stem cells via ultra-soft hydrogel for promoting angiogenesis, Compos. Part B-Eng. 234 (2022), 109747, https://doi.org/10.1016/j.compositesb.2022.109747.

[12] R. Goetzke, J. Franzen, A. Ostrowska, M. Vogt, A. Blaeser, G. Klein, B. Rath, H. Fischer, M. Zenke, W. Wagner, Does soft really matter? Differentiation of induced pluripotent stem cells into mesenchymal stromal cells is not influenced by soft hydrogels, Biomaterials 156 (2018) 147–158, https://doi.org/10.1016/j.biomaterials.2017.11.035.

[13] J.O. Buitrago, K.D. Patel, A. El-Fiqi, J.H. Lee, B. Kundu, H.H. Lee, H.W. Kim, Silk fibroin/collagen protein hybrid cell-encapsulating hydrogels with tunable gelation and improved physical and biological properties, Acta Biomater. 69 (2018) 218–233, https://doi.org/10.1016/j.actbio.2017.12.026.

[14] D. Chouhan, T.U. Lohe, P.K. Samudrala, B.B. Mandal, In situ forming injectable silk fibroin hydrogel promotes skin regeneration in full thickness burn wounds, Adv. Healthcare Mater. 7 (24) (2018), 1801092, https://doi.org/10.1002/adhm.201801092.

[15] F. Rizzo, N.S. Kehr, Recent advances in injectable hydrogels for controlled and local drug delivery, Adv. Healthcare Mater. 10 (1) (2021), 2001341, https://doi.org/10.1002/adhm.202001341.

[16] J. Wu, Z. Pan, Z.Y. Zhao, M.H. Wang, L. Dong, H.L. Gao, C.Y. Liu, P. Zhou, L. Chen, C.J. Shi, Z.Y. Zhang, C. Yang, S.H. Yu, D.H. Zou, Anti-swelling, robust, and adhesive extracellular matrix-mimicking hydrogel used as intraoral dressing, Adv. Mater. 34 (20) (2022), 2200115, https://doi.org/10.1002/adma.202200115.

[17] P. Fratzl, Collagen: structure and mechanics, an introduction, Collagen, Springer (2008) 1–13.

[18] Y.W. Zhan, W.J. Fu, Y.C. Xing, X.M. Ma, C.Y. Chen, Advances in versatile anti-swelling polymer hydrogels, Mater. Sci. Eng. C 127 (2021), 112208, https://doi.org/10.1016/j.msec.2021.112208.

[19] E. Prince, E. Kumacheva, Design and applications of man-made biomimetic fibrillar hydrogels, Nat. Rev. Mater. 4 (2) (2019) 99–115, https://doi.org/10.1038/s41578-018-0077-9.

[20] X.H. Zhao, X.Y. Chen, H. Yuk, S.T. Lin, X.Y. Liu, G. Parada, Soft materials by design: unconventional polymer networks give extreme properties, Chem. Rev. 121 (8) (2021) 4309–4372, https://doi.org/10.1021/acs.chemrev.0c01088.

[21] X. Zhang, L. Xiao, Z. Ding, Q. Lu, D.L. Kaplan, Engineered tough silk hydrogels through assembling β-sheet rich nanofibers based on a solvent replacement strategy, ACS Nano 16 (7) (2022) 10209–10218, https://doi.org/10.1021/acsnano.2c01616.

[22] M.D. Davidson, M.E. Prendergast, E. Ban, K.L. Xu, G. Mickel, P. Mensah, A. Dhand, P.A. Janmey, V.B. Shenoy, J.A. Burdick, Programmable and contractile materials through cell encapsulation in fibrous hydrogel assemblies, Sci. Adv. 7 (46) (2021), eabi8157, https://doi.org/10.1126/sciadv.abi8157.

[23] Z. Lin, X.M. Cheng, Synthesis and properties of pH sensitive carboxymethylated hydroxypropyl chitosan nanocarriers for delivery of doxorubicin, J. Macromol. Sci. 58 (9) (2021) 600–609, https://doi.org/10.1080/10601325.2021.1920332.

[24] Y.A. Zhao, Z.J. Wang, Q. Zhang, F.X. Chen, Z.Y. Yue, T.T. Zhang, H.B. Deng, C. Huselstein, D.P. Anderson, P.R. Chang, Y.P. Li, Y. Chen, Accelerated skin wound healing by soy protein isolate-modified hydroxypropyl chitosan composite films, Int. J. Biol. Macromol. 118 (2018) 1293–1302, https://doi.org/10.1016/j.ijbiomac.2018.06.195.

[25] X. Wang, X.-M. Cheng, Study on aggregation behavior of hydroxypropyl chitosan in aqueous solution, Chin. J. Anal. Chem. 43 (12) (2015) 1864–1869, https://doi.org/10.11895/j.issn.0253-3820.150416.

[26] A.K. Gaharwar, L.M. Cross, C.W. Peak, K. Gold, J.K. Carrow, A. Brokesh, K. A. Singh, 2D nanoclay for biomedical applications: regenerative medicine, therapeutic delivery, and additive manufacturing, Adv. Mater. 31 (23) (2019), 1900332, https://doi.org/10.1002/adma.201900332.

[27] Y.H. Kim, X. Yang, L.Y. Shi, S.A. Lanham, J. Hilborn, R.O.C. Oreffo, D. Ossipov, J. I. Dawson, Bisphosphonate nanoclay edge-site interactions facilitate hydrogel self-assembly and sustained growth factor localization, Nat. Commun. 11 (1) (2020) 1–9, https://doi.org/10.1038/s41467-020-15152-9.

[28] K. Yue, G. Trujillo-de Santiago, M.M. Alvarez, A. Tamayol, N. Annabi, A. Khademhosseini, Synthesis, properties, and biomedical applications of gelatin methacryloyl (GelMA) hydrogels, Biomaterials 73 (2015) 254–271, https://doi.org/10.1016/j.biomaterials.2015.08.045.

[29] J.M. Zatorski, A.N. Montalbine, J.E. Ortiz-Cardenas, R.R. Pompano, Quantification of fractional and absolute functionalization of gelatin hydrogels by optimized ninhydrin assay and H-1 NMR, Anal. Bioanal. Chem. 412 (24) (2020) 6211–6220, https://doi.org/10.1007/s00216-020-02792-5.

[30] A. Agah, T.R. Kyriakides, N. Letrondo, B. Bjorkblom, P. Bornstein, Thrombospondin 2 levels are increased in aged mice: consequences for cutaneous wound healing and angiogenesis, Matrix Biol. 22 (7) (2004) 539–547, https://doi.org/10.1016/j.matbio.2003.09.004.

[31] Z.H. Cheng, J. Huang, S. Hu, C.J. Jiang, Q. Ge, H.W. Lai, J.Y. Gong, P.L. Sun, J. W. Mao, L.H. Mei, Effects of hydroxypropyl degree on physiochemical activities of chitosan from squid pens, Int. J. Biol. Macromol. 65 (2014) 246–251, https://doi.org/10.1016/j.ijbiomac.2014.01.048.
[32] A.-L. Fameau, A. Salonen, Effect of particles and aggregated structures on the foam stability and aging, Compt. Rendus Phys. 15 (8–9) (2014) 748–760, https://doi.org/10.1016/j.crhy.2014.09.009.
[33] Y.J. Wang, X.N. Zhang, Y.H. Song, Y.P. Zhao, L. Chen, F.M. Su, L.B. Li, Z.L. Wu, Q. Zheng, Ultrastiff and tough supramolecular hydrogels with a dense and robust hydrogen bond network, Chem. Mater. 31 (4) (2019) 1430–1440, https://doi.org/10.1021/acs.chemmater.8b05262.
[34] B.O. Okesola, A.K. Mendoza-Martinez, G. Cidonio, B. Derkus, D.K. Boccorh, D.O. de la Pena, S. Elsharkawy, Y.H. Wu, J.I. Dawson, A.W. Wark, D. Knani, D.J. Adams, R. O.C. Oreffo, A. Mata, De novo design of functional coassembling organic-inorganic hydrogels for hierarchical mineralization and neovascularization, ACS Nano 15 (7) (2021) 11202–11217, https://doi.org/10.1021/acsnano.0c09814.
[35] A.M. Chuah, T. Kuroiwa, S. Ichikawa, I. Kobayashi, M. Nakajima, Formation of biocompatible nanoparticles via the self-assembly of chitosan and modified lecithin, J. Food Sci. 74 (1) (2009) N1–N8, https://doi.org/10.1111/j.1750-3841.2008.00985.x.
[36] Y.W. Zhan, W.J. Fu, Y.C. Xing, X.M. Ma, C.Y. Chen, Advances in versatile anti-swelling polymer hydrogels, Mater. Sci. Eng. C 127 (2021), 112208, https://doi.org/10.1016/j.msec.2021.112208.
[37] O. Okay, S.B. Sariisik, Swelling behavior of poly(acrylamide-co-sodium acrylate) hydrogels in aqueous salt solutions: theory versus experiments, Eur. Polym. J. 36 (2) (2000) 393–399, https://doi.org/10.1016/S0014-3057(99)00058-0.
[38] D.J. Page, C.E. Clarkin, R. Mani, N.A. Khan, J.I. Dawson, N.D. Evans, Injectable nanoclay gels for angiogenesis, Acta Biomater. 100 (2019) 378–387, https://doi.org/10.1016/j.actbio.2019.09.023.
[39] G. Kiaee, N. Dimitrakakis, S. Sharifzadeh, H.J. Kim, R.K. Avery, K.M. Moghaddam, R. Haghniaz, E.P. Yalcintas, N.R. de Barros, S. Karamikamkar, A. Libanori, A. Khademhosseini, P. Khoshakhlagh, Laponite-based nanomaterials for drug delivery, Adv. Healthcare Mater. 11 (7) (2022), 2102054, https://doi.org/10.1002/adhm.202102054.
[40] C. Creton, 50th anniversary perspective: networks and gels: soft but dynamic and tough, Macromolecules 50 (21) (2017) 8297–8316, https://doi.org/10.1021/acs.macromol.7b01698.
[41] D. Chimene, R. Kaunas, A.K. Gaharwar, Hydrogel bioink reinforcement for additive manufacturing: a focused review of emerging strategies, Adv. Mater. 32 (1) (2020), 1902026, https://doi.org/10.1002/adma.201902026.
[42] H.L. Mao, S.J. Zhao, Y.X. He, M. Feng, L.H. Wu, Y.Y. He, Z.W. Gu, Multifunctional polysaccharide hydrogels for skin wound healing prepared by photoinitiator-free crosslinking, Carbohydr. Polym. 285 (2022), 119254, https://doi.org/10.1016/j.carbpol.2022.119254.
[43] Z.J. Geng, Y.X. Ji, S. Yu, Q.F. Liu, Z.B. Zhou, C.P. Guo, D.H. Lu, D.T. Pei, Preparation and characterization of a dual cross-linking injectable hydrogel based on sodium alginate and chitosan quaternary ammonium salt, Carbohydr. Res. 507 (2021), 108389, https://doi.org/10.1016/j.carres.2021.108389.
[44] H. Fu, C.G. Yu, X.D. Li, H.Y. Bao, B. Zhang, Z.J. Chen, Z.J. Zhang, Facile engineering of ECM-mimetic injectable dual crosslinking hydrogels with excellent mechanical resilience, tissue adhesion, and biocompatibility, J. Mater. Chem. B 9 (48) (2021) 10003–10014, https://doi.org/10.1039/d1tb01914g.
[45] V.G. Muir, T.H. Qazi, S. Weintraub, B.O.T. Maldonado, P.E. Arratia, J.A. Burdick, Sticking together: injectable granular hydrogels with increased functionality via dynamic covalent inter-particle crosslinking, Small 18 (36) (2022), 2201115, https://doi.org/10.1002/smll.202201115.
[46] Z.M. Tang, F. Jiang, Y.H. Zhang, Y. Zhang, Y. Yang, X.L. Huang, Y.Y. Wang, D. D. Zhang, N. Ni, F. Liu, M. Luo, X.Q. Fan, W.A. Zhang, P. Gu, Mussel-inspired injectable hydrogel and its counterpart for actuating proliferation and neuronal differentiation of retinal progenitor cells, Biomaterials 194 (2019) 57–72, https://doi.org/10.1016/j.biomaterials.2018.12.015.
[47] W.T. Kang, B. Bi, R.X. Zhuo, X.L. Jiang, Photocrosslinked methacrylated carboxymethyl chitin hydrogels with tunable degradation and mechanical behavior, Carbohydr. Polym. 160 (2017) 18–25, https://doi.org/10.1016/j.carbpol.2016.12.032.
[48] Y.Q. Chen, W.B. Sheng, J.J. Lin, C.Z. Fang, J.P. Deng, P. Zhang, M. Zhou, P. Liu, J. Weng, F. Yu, D.L. Wang, B. Kang, H. Zeng, Magnesium oxide nanoparticle coordinated phosphate-functionalized chitosan injectable hydrogel for osteogenesis and angiogenesis in bone regeneration, ACS Appl. Mater. Interfaces 14 (6) (2022) 7592–7608, https://doi.org/10.1021/acsami.1c21260.
[49] Y.Q. Chen, A. Udduttula, X.L. Xie, M. Zhou, W.B. Sheng, F. Yu, J. Weng, D.L. Wang, B. Teng, G. Manivasagam, J.V. Zhang, P.G. Ren, B. Kang, H. Zeng, A novel photocrosslinked phosphate functionalized Chitosan-Sr5(PO4)(2)SiO4 composite hydrogels and in vitro biomineralization, osteogenesis, angiogenesis for bone regeneration application, Compos. Part B-Eng. 222 (2021), 109057, https://doi.org/10.1016/j.compositesb.2021.109057.
[50] M. Alizadehgiashi, C.R. Nemr, M. Chekini, D.P. Ramos, N. Mittal, S.U. Ahmed, N. Khuu, S.O. Kelley, E. Kumacheva, Multifunctional 3D-printed wound dressings, ACS Nano 15 (7) (2021) 12375–12387, https://doi.org/10.1021/acsnano.1c04499.
[51] J.H. Teoh, A. Mozhi, V. Sunil, S.M. Tay, J. Fuh, C.W. Wang, 3D printing personalized, photocrosslinkable hydrogel wound dressings for the treatment of thermal burns, Adv. Funct. Mater. 31 (48) (2021). ARTN.2105932.10.1002/adfm.202105932.
[52] B. Kessel, M. Lee, A. Bonato, Y. Tinguely, E. Tosoratti, M. Zenobi-Wong, 3D bioprinting of macroporous materials based on entangled hydrogel microstrands, Adv. Sci. 7 (18) (2020), 2001419, https://doi.org/10.1002/advs.202001419.
[53] H. Zhang, Y. Cong, A.R. Osi, Y. Zhou, F.C. Huang, R.P. Zaccaria, J. Chen, R. Wang, J. Fu, Direct 3D printed biomimetic scaffolds based on hydrogel microparticles for cell spheroid growth, Adv. Funct. Mater. 30 (13) (2020), 1910573, https://doi.org/10.1002/adfm.201910573.
[54] A.K. Gaharwar, S.M. Mihaila, A. Swami, A. Patel, S. Sant, R.L. Reis, A.P. Marques, M.E. Gomes, A. Khademhosseini, Bioactive silicate nanoplatelets for osteogenic differentiation of human mesenchymal stem cells, Adv. Mater. 25 (24) (2013) 3329–3336, https://doi.org/10.1002/adma.201300584.
[55] J.K. Carrow, L.M. Cross, R.W. Reese, M.K. Jaiswal, C.A. Gregory, R. Kaunas, I. Singh, A.K. Gaharwar, Widespread changes in transcriptome profile of human mesenchymal stem cells induced by two-dimensional nanosilicates, Proc. Natl. Acad. Sci. USA 115 (17) (2018) E3905–E3913, https://doi.org/10.1073/pnas.1716164115.
[56] Z. Zhang, W. Li, Y. Liu, Z. Yang, L. Ma, H. Zhuang, E. Wang, C. Wu, Z. Huan, F. Guo, J. Chang, Design of a biofluid-absorbing bioactive sandwich-structured Zn-Si bioceramic composite wound dressing for hair follicle regeneration and skin burn wound healing, Bioact. Mater. 6 (7) (2021) 1910–1920, https://doi.org/10.1016/j.bioactmat.2020.12.006.
[57] S.F. Zhao, Q.H. Jiang, S. Peel, X.X. Wang, F.M. He, Effects of magnesium-substituted nanohydroxyapatite coating on implant osseointegration, Clin. Oral Implants Res. 24 (A100) (2013) 34–41, https://doi.org/10.1111/j.1600-0501.2011.02362.x.
[58] N. Zandi, B. Dolatyar, R. Lotfi, Y. Shallageh, M.A. Shokrgozar, E. Tamjid, N. Annabi, A. Simchi, Biomimetic nanoengineered scaffold for enhanced full-thickness cutaneous wound healing, Acta Biomater. 124 (2021) 191–204, https://doi.org/10.1016/j.actbio.2021.01.029.
[59] L. Zheng, B. Gu, S.S. Li, B.C. Luo, Y.M. Wen, M.W. Chen, X.Y. Li, Z.A. Zha, H. T. Zhang, X.Y. Wang, An antibacterial hemostatic AuNPs@corn stalk/chitin composite sponge with shape recovery for promoting wound healing, Carbohydr. Polym. 296 (2022), 119924, https://doi.org/10.1016/j.carbpol.2022.119924.